International Journal of Greenhouse Gas Control 109 (2021) 103387

Contents lists available at ScienceDirect

International Journal of Greenhouse Gas Control

journal homepage: www.elsevier.com/locate/ijggc

Quantification of dissolved CO_2 plumes at the Goldeneye CO_2-release experiment

Jonas Gros [a,*], Mark Schmidt [a], Peter Linke [a], Saskia Dötsch [a,1], Jack Triest [b], María Martínez-Cabanas [a], Mario Esposito [a], Andrew W. Dale [a], Stefan Sommer [a], Anita Flohr [c,d], Joseph Fone [c], Jonathan M. Bull [c], Ben Roche [c], James A. Strong [d], Kevin Saw [d], Robin Brown [d], Dirk Koopmans [e], Klaus Wallmann [a]

[a] GEOMAR Helmholtz Centre for Ocean Research Kiel, Wischhofstr. 1-3, D-24148 Kiel, Germany
[b] 4H-JENA engineering GmbH, Wischhofstraße 1-3, (Gebäude 4), D-24148 Kiel, Germany
[c] University of Southampton, Waterfront Campus, European Way, SO14 3ZH Southampton, UK
[d] National Oceanography Centre Southampton, European Way, SO14 3ZH Southampton, UK
[e] MPI for Marine Microbiology, Celsiusstr. 1, D-28359 Bremen, Germany

ARTICLE INFO

Keywords:
Carbon dioxide (CO_2)
Carbon Capture and Storage (CCS)
Marine CO_2 leak detection
Marine CO_2 leak quantification
Offshore CCS monitoring
CO_2 leak simulations

ABSTRACT

According to many prognostic scenarios by the Intergovernmental Panel on Climate Change (IPCC), a scaling-up of carbon dioxide (CO_2) capture and storage (CCS) by several orders-of-magnitude is necessary to meet the target of $\leq$2 °C global warming by 2100 relative to preindustrial levels. Since a large fraction of the predicted CO_2 storage capacity lies offshore, there is a pressing need to develop field-tested methods to detect and quantify potential leaks in the marine environment. Here, we combine field measurements with numerical models to determine the flow rate of a controlled release of CO_2 in a shallow marine setting at about 119 m water depth in the North Sea. In this experiment, CO_2 was injected into the sediment at 3 m depth at 143 kg d^{-1}. The new leakage monitoring tool predicts that 91 kg d^{-1} of CO_2 escaped across the seafloor, and that 51 kg d^{-1} of CO_2 were retained in the sediment, in agreement with independent field estimates. The new approach relies mostly on field data collected from ship-deployed technology (towed sensors, Acoustic Doppler current profiler—ADCP), which makes it a promising tool to monitor existing and upcoming offshore CO_2 storage sites and to detect and quantify potential CO_2 leakage.

1. Introduction

Carbon dioxide (CO_2) capture and storage (CCS) represents a major contribution in some of the scenarios predicted to restrict global warming to $\leq$2 °C by 2100 relative to preindustrial levels (IPCC, 2018, 2005). CCS involves capturing CO_2 chiefly from large point sources and injecting it into subsurface geologic reservoirs to keep this greenhouse gas outside of either the atmosphere or the hydrosphere for the next hundred years or more (Dean et al., 2020; Hepple and Benson, 2005; IPCC, 2005). The foreseen CO_2 storage capacity lies largely offshore, both worldwide (Ringrose and Meckel, 2019) and in Europe (EU Geo-Capacity, 2009). However, ensuring safe and climate-efficient large-scale adoption of the technology at up to 16 Gt y^{-1} of CO_2 injected by 2050 (IPCC, 2018) requires the availability of field-tested methods to detect, attribute, and quantify potential leaks (Dixon and Romanak, 2015).

Offshore CO_2-leakage detection in shallow shelf seas is challenging due to strong currents, tides, and meteorological influences especially at relatively shallow water depths. Moreover, seawater alkalinity and its variability (Millero, 2007; Zeebe and Wolf-Gladrow, 2001), fast CO_2 bubble dissolution rates (Beaubien et al., 2014; Gros et al., 2019; McGinnis et al., 2011; Uchimoto et al., 2020), carbonate system kinetics (Koopmans et al., 2021; Schulz et al., 2006), and natural variability of the carbon cycle (Blackford et al., 2017) complicate identification of CO_2 anomalies (measured from partial pressure of CO_2, pCO_2, or from pH) and leakage source localization in the water column. Near- and

* Corresponding author at: GEOMAR Helmholtz centre for Ocean Research Kiel, RD2 / Marine Geosystems, Wischhofstr. 1-3, D-24148 Kiel, Germany.
E-mail address: jogros@geomar.de (J. Gros).
[1] present address: Fachklinik Aukrug, Tönsheide 10, D-24613 Aukrug, Germany.

https://doi.org/10.1016/j.ijggc.2021.103387
Received 23 December 2020; Received in revised form 21 May 2021; Accepted 15 June 2021
Available online 28 June 2021

far-field water chemistry in coastal areas can be investigated by using e.g., divers, small vessel mounted devices, and small remotely operated and autonomous underwater vehicles (Beaubien et al., 2014; Blackford et al., 2015; Flohr et al., 2021a; Taylor et al., 2015; Totland et al., 2020). However, when monitoring seafloor installations or reservoir integrity far offshore, large vessels and heavy offshore technology is usually needed (Wallmann et al., 2015).

Numerical simulations of CO_2 leakage in the marine environment have determined the dissolution and dispersion of this particularly soluble gas in the sea. Aqueous dissolution of CO_2 gas is expected to happen within meters from the seafloor under most circumstances (Dewar et al., 2015, 2013; Gros et al., 2019; McGinnis et al., 2011; Vielstädte et al., 2019), and even major blowouts at water depths greater than 50 m are expected to dissolve completely (Oldenburg and Pan, 2019). These findings are further corroborated by field observations during release experiments and at natural seep sites (Beaubien et al., 2014; Gros et al., 2019; Uchimoto et al., 2020; Vielstädte et al., 2019). Since measurements using sensors and other techniques are necessarily patchy in a rapidly changing environment (e.g., tidal currents, storm events), models are useful in enabling prediction of the temporal and spatial distribution of CO_2-affected water around one or several release locations (Blackford et al., 2013; Gros et al., 2019; Phelps et al., 2015; Vielstädte et al., 2019). However, to date, most modeling studies have focused on either theoretical scenarios or have chiefly used field data collected during controlled or natural active CO_2 release to validate simulations. These studies have improved the scientific understanding, but are not leakage-monitoring tools. In order to quantify leakage, a tighter coupling of field data and simulation tools is needed to investigate field leakage sites and to determine source strengths.

Recent developments of towed video-controlled subsea platforms such as the Video-CTD water sampler rosette provide a technology to investigate natural offshore CO_2 seepage by using standard coaxial winch cables even when operating from a vessel without dynamic positioning (DP) (McGinnis et al., 2011; Schmidt et al., 2015). The Video-CTD includes a variety of sensors that provide real-time data, and the technology has been proven to allow for successful monitoring and quantification of gas release from the seafloor up to the atmosphere at a man-made gas blowout in the North Sea (Sommer et al., 2015). In situ dissolved CO_2 measurements performed with the Video-CTD have been combined with current detection and plume transport modeling to quantify CO_2 leakage (Gros et al., 2019). However, the latter studies were applied to settings where the leakage magnitude could not be ascertained independently of their estimations, and it is therefore desirable to apply these tools to field-scale conditions where the CO_2 source strength and locations are known.

To apply and further develop the existing leakage detection technology (McGinnis et al., 2011; Schmidt et al., 2015) and gas dissolution and transport modeling software (Gros et al., 2019), we used data collected during a joint research campaign with *RV Poseidon* (POS534 cruise) and *RRS James Cook* (JC180 cruise) in May 2019. The campaign was conducted in the North Sea near the Goldeneye offshore platform (Flohr et al., 2021a). There, a CO_2/tracer-release experiment was conducted at the seafloor from onboard the *RSS James Cook* (Connelly et al., 2019). The controlled release of gas into the surface sediment and the resulting emission into the bottom water was monitored, among others, with sensors towed from the *RV Poseidon* (Schmidt, 2019). This study demonstrates that a combined system composed of towed sensor data and a simulation tool enables leak detection and provides an accurate estimate of leak flow rate.

2. Methods

2.1. Study site and CO_2 release experiment

The study area was situated 100 km offshore Scotland (east-northeast of Peterhead) and about 900 m SSE of the Goldeneye platform (Fig. 1). The area exhibits a flat seafloor at ~119 m water depth, and the surface sediment mainly consists of poorly-sorted muddy sand with a major mode grain size of ~63 μm (Dale et al., 2021).

To test the ability to detect and quantify CO_2 escape into the water column, as well as newly designed instruments and methods, a field CO_2-release experiment was conducted at the study site during May

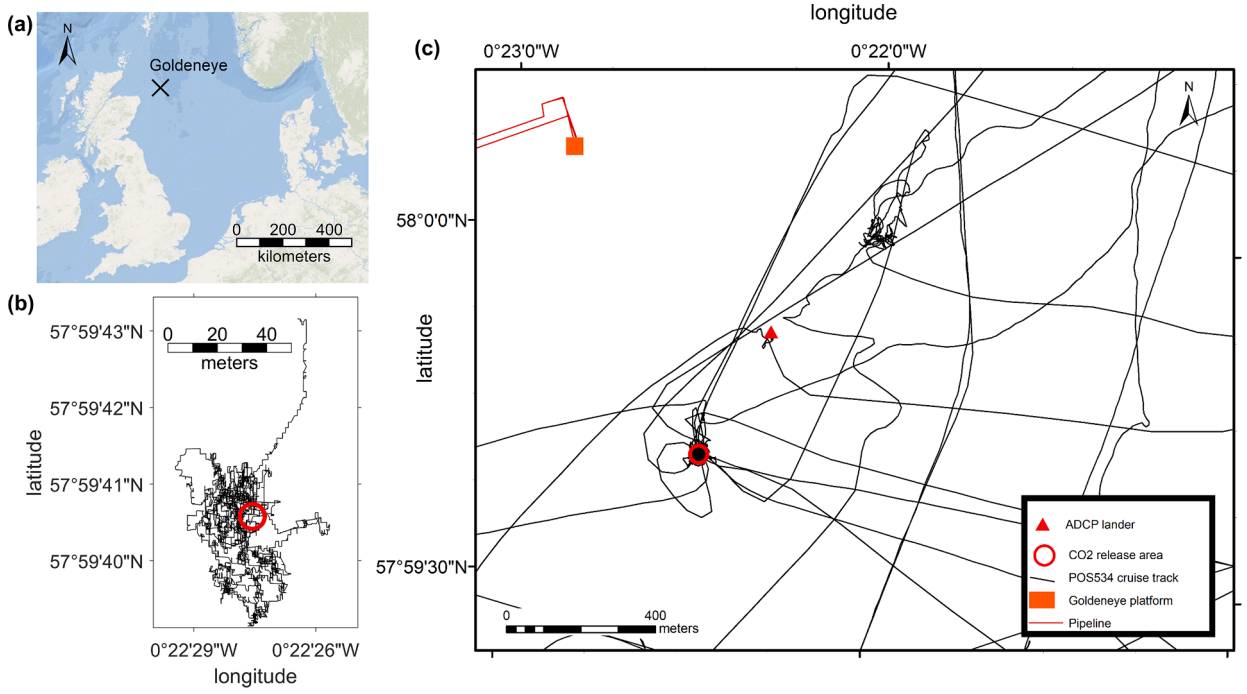

Fig. 1. (a) Location of the Goldeneye experimental site in the North Sea. (b) Video-CTD track in bottom water during visit 3; the red circle is centered on the area of gas release. (c) Working area southeast of Goldeneye platform. The CO_2-release site is marked by the red circle, the ADCP lander by the red triangle, and the track of RV Poseidon is marked by the black solid line.

11–22, 2019 involving two research vessels: the *RV Poseidon* and the *RRS James Cook* (Flohr et al., 2021a). A customized gas injection system was deployed, which released CO_2 and a mixture of tracer gases at 3 m below the seafloor, at a flow rate that was increased in a series of steps from 6 to 143 kg d^{-1} (Flohr et al., 2021a). The released gas was predominantly CO_2 (99.99% on a molar basis), containing traces of methane (CH_4, 45 ppm) as well as the added tracer gases krypton (Kr, 59 ppm), sulfur hexafluoride (SF_6, 1.8 ppm), and octafluoropropane (C_3F_8, 0.11 ppm). The leakage of a fraction of the released gas at the sediment-water interface was monitored with a variety of scientific equipment. Further details of the experimental set-up are described in a different article within the present special issue (Flohr et al., 2021a).

2.2. Continuous monitoring and sampling device

A multipurpose Video-CTD (Linke et al., 2015; Schmidt et al., 2015) deployed from *RV Poseidon* was used to detect pCO_2 anomalies in the water column above the CO_2-release site. The Video-CTD was towed mid-ships in bottom view mode (~1–5 m above seafloor) at low speed (0.2–1 knot) following a random track pattern aimed to be centered on the release site. Four deployments of the instrument were conducted, termed here pre-injection, visit 1, visit 2, and visit 3 (Table 1). The sensors measuring in situ pCO_2 were a commercial infrared absorption sensor with a pumped flow-through membrane head (HydroC-CO_2, Kongsberg Maritime Contros GmbH, currently distributed by 4H Jena Engineering GmbH). Calibration of the sensors (100–3000 µatm) was performed before and after the cruise in Kiel using a reference detector calibrated with reference materials. Field deployments enabled determination of an initial accuracy of ±0.5%. The sensor used (serial number: 0412–005) had a 63% response time (t_{63}) of 140 s, leading to a recorded signal not representative of the instantaneous pCO_2 in the monitored water. Therefore, after return onshore, the raw sensor signal was smoothed (using a Gaussian filter having a 70-s width) and corrected for the sensor response time (Atamanchuk et al., 2015; Miloshevich et al., 2004), such that the instantaneous concentrations were retrieved. Standard pH (SBE27, Sea-Bird Scientific), pressure, temperature, and conductivity sensors (SBE 9 plus, Sea-Bird Scientific), oxygen sensor (SBE43, Sea-Bird Scientific), altimeter (PSA-916, Teledyne Benthos), pCH_4 (HydroC-CH_4, Kongsberg Maritime Contros GmbH, currently distributed by 4H Jena Engineering GmbH), and pCO_2 (serial number: 0412–005) sensors were all attached to the Video-CTD frame at the same height (Fig. 2a). A second pCO_2 sensor (serial number: 0119–001) was mounted on the Video-CTD with the inlet at the top of the Video-CTD frame, 1.5 m above the sensor 0412–005. Sensor measurements are further discussed in a companion manuscript (Martínez-Cabanas et al., 2021), whereas here we focus on how the collected data can be combined with a model tracking bubble dissolution and dissolved CO_2 transport (Gros et al., 2019) to enable leakage rate quantification.

All in situ sensor measurements were recorded online and were related to the ship's navigation data and weather data. Moreover, 10 water samples taken by Niskin-bottles at selected locations were analyzed after recovery of the Video-CTD and are discussed elsewhere (Martínez-Cabanas et al., 2021). Live video-streams and images were recorded on the onboard computer and on internal camera memory in HD quality to monitor gas bubble streams emanating from the seafloor and to locate and mark scientific installations at the release site (Fig. 2b).

2.3. Water currents

Water current data were recorded with a 300 kHz ADCP-lander system deployed at 350 m to the NNE of the CO_2-release site at Goldeneye (Fig. 1) (Schmidt, 2019). A trawl-resistant lander (TRL AL-200, Flotation Technologies) was deployed at 06:57 on May 10 at a water depth of 122 m and recovered at 12:13 on May 25. In addition to the upward-looking ADCP (300 kHz, Teledyne RDI), the lander included a CTD (SBE 37IM, Sea-Bird Scientific), and pH and CO_2 sensors (University of Technology Graz) (Esposito et al., 2021). The ADCP recorded data at a 5-min interval, using a 1-m vertical bin with a first bin centered at 3.2 m above seafloor (masf). In order to properly resolve water currents close to the seafloor, an acoustic Doppler velocimeter (ADV) mounted on a fiberglass frame recorded the water current at 0.16 masf at the experimental site (Koopmans et al., 2021); the ADV had a high sampling rate (16 Hz), which enabled capture of turbulent water movement, used to estimate the relative magnitude of horizontal and vertical diffusion coefficients (Section 2.7.2). The ADV data were combined with the data of the ADCP lander, and smoothing was performed for simulation purposes in order to remove ADCP and ADV instrument noise and contributions from unresolved turbulence. Because the CO_2 dissolution happened close to the seafloor, water current direction was calculated as the average ADCP direction over 3.2–20 masf, for each time step. The water current intensity was assumed to follow the law of the wall, fitted to the combined ADV and ADCP data within 0.16–20 masf (i.e., $U(z) = C_1 + C_2 \cdot \log_{10}(z_0\text{-}z)$, where C_1 and C_2 are two fitted parameters, z_0 is the total water depth, z is the water depth, and U is the water current intensity). Water currents in the simulations were linearly interpolated/extrapolated (in time and space). The 0.16 masf measurement was missing on May 19–20 during visit 3 (sensor biofouling), and was replaced by an estimate from readings at 3.2 masf using data from the ADCP-lander and correlations fitted to the available (non-biofouled) data (Supporting Information Figure S1, $U_N(0.16\ masf) = 0.657 \cdot U_N(3.2\ masf) + 0.01029$ and $U_E(0.16\ masf) = 0.558 \cdot U_N(3.2\ masf) - 0.0117$, where U_N and U_E are the water current velocities in m s^{-1} in the north and east direction, respectively).

2.4. Initial gas bubble size distribution

Optical data were collected by placing a specialist lander directly over a seep on May 15, 2019 when gas was being injected into the seafloor at a rate of 29 kg d^{-1}. Footage was collected using a SONY FDR-X3000 Action Camera at 30 fps in 720p. Image analysis was performed using a custom script, detailed in Li et al., 2021, which was used to measure the size of bubbles escaping the seep. The approach taken was to derive and subtract a background image from the video leaving only the bubbles. The area of the bubbles is then averaged over a number of frames at ~ 0.5 masf before a volume of revolution calculation is performed to estimate the total volume of the bubbles. By assuming these volumes of gas represent a spherical bubble, equivalent bubble radiuses are then determined.

Table 1
Station data (Schmidt, 2019) and experimental CO_2-flow rate constraints (Connelly et al., 2019).[a]

station name	date	total deployment period (UTC)	CO_2 release flow rate at 3-m depth into the sediment (kg d^{-1})
pre-injection	10.05.2019	08:00–15:00	0 (Natural background)
visit 1	13/14.05.2019	16:50–03:00	6
visit 2	16/17.05.2019	18:00–03:40	29
visit 3	19/20.05.2019	20:50–04:50	143

[a] only data collected within 10 masf were assumed potentially influenced by the experimentally-released CO_2 and were used for leakage rate estimate.

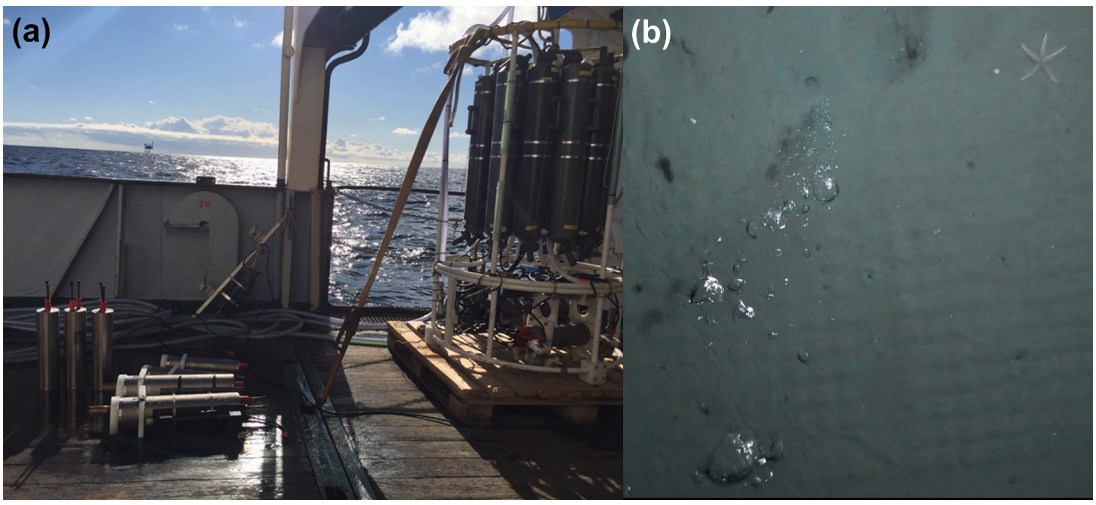

Fig. 2. (a) Sea-Bird water sampler (10×10 L Niskin) rosette including SBE9plus CTD, pH/Oxydation Reduction Potential (O.R.P.) sensor (SBE27), O_2, and altimeter sensors. External power-packs and 2x HydroC™-CO_2 and 2x HydroC™-CH_4 on the left side are ready to be mounted to the rosette frame. Downward looking video/illumination devices and respective data and power handling is described in Linke et al. (2015). (b) Picture of a gas bubble stream taken by the Video-CTD during visit 3.

2.5. Gas sampling and analysis

The performance of the bubble ascent and dissolution model (Section 2.7.1), was tested by monitoring the changes in trace gas composition (C_3F_8, SF_6, Kr and CH_4) and the ^{13}C isotope content of CO_2 in gas bubbles sampled from individual bubble streams at different heights above seafloor. Gas bubbles were sampled using gas bubble samplers (Corsyde, Germany) that were operated by the remotely operated vehicle (ROV) manipulator arms. The gas bubble samplers consisted of an inverted transparent funnel (0.7 L internal volume), inlet valve, stainless steel sample cylinder (0.5 L internal volume) and outlet valve. To quantify the rates of CO_2 dissolution in the water column, gas bubbles were sampled at ~0.10–0.15 masf and from higher in the water column (ranging from 0.9 to 2.7 masf). A flow-through Fourier-Transmission Infra-Red (FTIR) analyser (atmosFIR, Protea Ltd., UK) was used on board the vessel to measure CO_2, CH_4, SF_6, and C_3F_8 concentrations. The isotopic composition of the discrete gas samples ($\delta^{13}C$ of CO_2) was determined after the experiment using a Delta V Advantage isotope ratio mass spectrometer fitted with a Gas Bench II (Thermo Fisher Scientific). More detailed description of the gas sampling and analysis can be found in Flohr et al., (2021b).

2.6. Data processing procedures

2.6.1. Altimeter and water depth sensor data

The Video-CTD included both a water depth sensor and an altimeter. Occasional aberrant readings from the altimeter were interpolated as described in Supporting Information (SI) section S2. The estimated precision (~ 2 standard deviations, 2σ) of the recorded altitude above seafloor is ±20 cm.

2.6.2. Estimation of the geographic coordinates of the Video-CTD at depth

The recorded coordinates during the research cruise corresponded to the position of the ship's Furuno F150 GPS receiver, which was located ~10 m, horizontally, from the point of entry in water of the Video-CTD cable. The geographical coordinates of the point of entry in water of the cable were calculated from the known positions on the ship. However, processes such as water currents were estimated to have displaced the instrument by up to 17 m horizontally at the local water depth of 119 m. The recorded videos during visit 3 ascertained that the instrument was towed a total of six times over a benthic chamber, which was part of the release experiment and maintained a fixed position on the seafloor. The extent of lateral drift incurred by the water current on the Video-CTD was estimated using the position of entry in water of the Video-CTD cable at the sea surface and the average water current within the three first bins above the seafloor:

$$\overrightarrow{\Delta x}(t) = 50 \cdot \overrightarrow{u}(t) \quad (1)$$

where $\overrightarrow{\Delta x}$ is the horizontal displacement vector (m) of the Video-CTD subsea relative to the point of entry in water incurred by water currents at time t, and $\overrightarrow{u}$ is the average water current vector (m s^{-1}) calculated over the three lowest ADCP bins at time t. The value of the coefficient (50 s) was determined such as to minimize the average distance between the estimated positions of the Video-CTD at the seafloor when the benthic chamber was visible on the videos (SI section S3). This procedure led to an estimated horizontal precision of the Video-CTD position at ~119 m water depth of ±2.5 m. Better precision is unlikely to be achieved with the accuracy of the GPS (several meters).

2.6.3. Baseline pCO_2 signal

The towed sensors mainly moved within water unaffected by the released gas (i.e., baseline pCO_2 signal), showing narrow peaks when the sensors were flushed with waters affected by the released CO_2, corresponding to a signal increase compared to the baseline, which lasted typically approximately 90 s. As a complicating factor, the baseline pCO_2 signal oscillated slightly with time. Since the aim was to estimate CO_2 leakage rate by minimizing the difference between field measurements and simulations, knowledge of the time-dependent baseline pCO_2 signal was required, so that the source strength estimate depended on the pCO_2 peaks with minimized interference from baseline. The simulated pCO_2 signal was calculated based on the simulated time- and space-dependent excess dissolved inorganic carbon (excess DIC) arising from the release and the time-dependent baseline pCO_2 signal, assuming constant total alkalinity. Accurate estimation of the baseline signal is particularly important for leakage rate estimation at low flow rates where the measured deviations from baseline are expected to be small. The baseline pCO_2 signal was estimated using the Matlab algorithm of Eilers, which is designed to track the base of peaks using asymmetric least square fitting (Eilers, 2004).

The algorithm of Eilers used includes three parameters which together determine the smoothness of the estimated baseline (section S4). Here, the parameters selected were $p = 0.003$, $\lambda = 10^9$, and $d = 2$ to estimate the temporal evolution of the baseline pCO_2 in absence of the

excess signal resulting from the experimental release. Finally, owing to its asymmetric least square approach, the algorithm of Eilers tended to follow the bottom of the noise of the baseline rather than the center of the noise. An offset between Eilers's baseline and the center of the noise was calculated from a sequence of measured data with no deviation from baseline, and the corresponding offset factor was applied to all the dataset to ensure that the baseline tracked the middle of the noise in absence of experimentally-released CO_2 (Fig. 8).

2.7. Simulations and estimation of the CO_2 flow rate exiting the surface sediments

A gas dissolution and transport model (Gros et al., 2019) was modified to simulate the dissolution of emitted gas bubbles and the subsequent advection and dispersion of the excess DIC, as well as the equilibrium CO_2 carbonate chemistry. The initial bubble size distribution at the seafloor was assumed independent of gas flow rate, and density currents were unlikely to be generated at the concentrations involved (Gros et al., 2019; Vielstädte et al., 2019). Thus the simulated excess DIC in the water column depended linearly on the gas leakage flow rate at the seafloor. This linear dependence was used to estimate the source strength (flow rate of CO_2 gas exiting the seafloor) by minimizing the difference between simulated pCO_2 values and field measurements (Section 2.2).

In order to estimate the gas flow rate exiting the seafloor, the model was fit to the readings of a pCO_2 sensor towed according to the known trajectory of the Video-CTD (Section 2.6.2) within the simulated domain. The CO_2 flow rate out of the sediment that minimized the sum of the absolute values of the difference between the simulated and measured detector signal was considered the best-estimate flow rate, which was then compared to the known flow rate of CO_2 injected into the sediment (Section 3.3) and to published estimates based on different methods (Section 4.2). The model was implemented in Matlab, Python, and Fortran, with the user interacting with the model via Matlab. The results reported here used Matlab version R2019a and Python version 2.7.13.

The model includes three different modules, described below.

2.7.1. Bubble (plume) model

The bubble plume model was used to simulate the ascent of bubbles exiting the seafloor, assumed to have an initial size distribution at the emission source as optically measured during the experiment (Section 2.4). The ascent trajectory of bubbles, mass transfer across the gas-water interface of the involved chemical species (CO_2, $^{13}CO_2$, CH_4, Kr, SF_6, C_3H_8, N_2, O_2, and Ar), and resulting bubble size evolution as a function of total bubble mass, pressure, temperature, and composition were simulated using the Texas A&M Oil spill (Outfall) Calculator (TAMOC) version 1.1.1 (Dissanayake et al., 2018; Gros et al., 2016, 2017), using chemical properties listed in Table S1.

The TAMOC model was previously validated for various gases based on laboratory and field data ranging from ~1 m to 1500 m water depth (Dissanayake et al., 2018; Gros et al., 2016, 2017,2019, 2020; Jun, 2018; Leonte et al., 2018; Razaz et al., 2020; Socolofsky et al., 2020; Wang et al., 2020). The model includes the Peng-Robinson equation of state and is able to predict densities and solubilities of gas mixtures and liquid hydrocarbon mixtures at the range of pressure, temperature, and salinity conditions present in global oceans (≤10,000 m water depth, salinity of ~35, temperatures of −2 °C to 30 °C) Gros et al. (2016).

Mass transfers were calculated according to (McGinnis et al., 2006):

$$\frac{dm_i}{dt} = -A\cdot\beta_i\cdot\left(C^{eq}_{w,i} - C_{w,i}\right) \tag{2}$$

where: m_i is the total mass of compound i in the bubble; A is the surface area of the bubble; β_i is the mass transfer coefficient (units: length time^{-1}) of compound i at the gas-water interface; $C^{eq}_{w,i}$ is the aqueous concentration of compound i at equilibrium with the gas composition; and $C_{w,i}$ is the modeled aqueous concentration of compound i in the seawater adjacent to the bubble. Properties of bubbles—including shape, surface area, slip velocity, and β_i—were estimated based on published formulae (Clift et al., 1978; Johnson et al., 1969), as explained previously Gros et al., 2017.

Gas bubbles were assumed to exhibit circulating interfaces (i.e., constantly renewed) in agreement with assumptions made by previous studies for gas bubbles in the sea (e.g., Dewar et al., 2013; Gros et al., 2019; McGinnis et al., 2011; Rehder et al., 2009; Vielstädte et al., 2015; Zheng and Yapa, 2002). The interfacial tension between the seawater and gas bubbles was assumed equal to the surface tension of seawater at ambient conditions (Sharqawy et al., 2010). The profile of O_2 concentrations in the water column was measured, and a pCH_4 value of 4 ppm was assumed in the lower water column based on measurements from the sensor mounted on the Video-CTD. Additionally, it was assumed that the concentrations of the non-reactive gases N_2, Ar, C_3F_8, SF_6, and Kr in the water column were at atmospheric saturation (Hamme and Emerson, 2004; McGinnis et al., 2006; Pilson, 2013). This latter assumption was deemed appropriate even for the anthropogenic C_3F_8 and SF_6 gases because of the shallow water depth leading to rapid equilibration with the atmosphere, including the presence of a yearly mixing period (Esposito et al., 2021).

In the simulations, bubbles were assumed to exit the seafloor with equal flow rate from each of the 8 observed bubble stream origins, which were recorded to have moderate to high flow rates during a ROV survey on May 21. Gas flow rates quantified for individual bubble streams by timing the filling of an inverted funnel (up to 0.52 L min^{-1}, Flohr et al., 2021b) were low compared to a flow rate experimentally confirmed to generate a bubble plume near Panarea Island (9.3 L min^{-1}, Gros et al., 2019). Thus it was assumed that the gas flow rates were weak and did not generate buoyant bubble plumes (Socolofsky and Adams, 2002; Wüest et al., 1992).

2.7.2. Dissolved CO_2 Lagrangian advection-dispersion model

Simulation of the fate of aqueous CO_2 was achieved with a previously tested Lagrangian advection and random-walk model (Gros et al., 2019), which was further refined here. The continuous concentration field was simulated by tracking discrete Lagrangian parcels of dissolved CO_2 having a three-dimensional position and infinitesimal size. Integration of millions of tracked Lagrangian parcels over an Eulerian grid of cells provided the concentration field at chosen time points. The near-field bubble simulation (Section 2.7.1) was performed with TAMOC and provided the 3-D mass flow rate of excess DIC entering the sea as a function of time and position above each simulated emission site. The simulated input of excess DIC to the water column above the emission sites depended on the instantaneous measured water velocity profile, which was assumed horizontally constant over the spatial model domain, and was interpolated from (smoothed) current measurements performed at a 5-min interval. At each simulated emission source, the input of dissolved CO_2 to the water column from ascending bubbles was discretized in thirty vertical bins. 40 Lagrangian parcels of dissolved CO_2 were released for each bin at each time step. The earlier model version (Gros et al., 2019) was further refined to enable a depth-dependent diffusion coefficient profile (Ross and Sharples, 2004), and horizontal diffusion coefficients parallel and perpendicular to the water current. The displacement of the dissolved-CO_2 parcels follow:

$$\Delta x = U_E\cdot\Delta t + \left(rand\cdot\sqrt{2\cdot D_{\parallel}(z)\cdot\Delta t}\right)\cdot sin(\alpha) + \left(rand\cdot\sqrt{2\cdot D_{\perp}(z)\cdot\Delta t}\right)\cdot cos(\alpha) \tag{4}$$

$$\Delta y = U_N\cdot\Delta t + \left(rand\cdot\sqrt{2\cdot D_{\parallel}(z)\cdot\Delta t}\right)\cdot cos(\alpha) + \left(rand\cdot\sqrt{2\cdot D_{\perp}(z)\cdot\Delta t}\right)\cdot sin(\alpha) \tag{5}$$

$$\Delta z = D_z'(z)\cdot\Delta t + \text{rand}\cdot\sqrt{2\cdot D_z\left(z + 0.5\cdot D_z'(z)\cdot\Delta t\right)\cdot\Delta t} \quad (6)$$

where Δx, Δy, and Δz are the displacements of a parcel over one time step in the x (east), y (north), and z (vertical) directions, respectively; Δt is the time step (1 s for the simulations reported here); *rand* is a normally-distributed random number having a mean of 0 and standard deviation of 1; U_E and U_N are the water current velocities interpolated at the time and depth of interest in the east and north direction, respectively; $D_{\parallel}$ and $D_{\perp}$, are the horizontal turbulent diffusion coefficients along and perpendicular to the water current, respectively, and D_z is the turbulent diffusion coefficient in the z direction; D_z' is the derivative of D_z with respect to depth; and α is the angle between the water current direction and the east ($sin(\alpha) = U_N/\sqrt{U_N^2 + U_E^2}$ and $cos(\alpha) = U_E/\sqrt{U_N^2 + U_E^2}$). The terms involving the derivative of D_z ensure correct consideration of the depth dependence of D_z (Ross and Sharples, 2004). The seafloor was simulated as a reflective wall boundary, and a random mixed layer was assumed for reflection at the seafloor (Ross and Sharples, 2004).

At time points of interest, excess DIC concentration relative to the time-dependent background DIC concentration observed in the field (Section 2.6.3) was calculated by integration of the mass of the Lagrangian parcels over a spatial grid. The chosen cell size is a tradeoff between resolution and the number of parcels of dissolved CO_2 that were tracked without reaching the computer memory limit (16 GB of RAM). To decrease the memory requirement, particles exiting a selected spatial range (plotted in Fig. 6) by more than 20-m distance were immediately "forgotten" by the Lagrangian model, which simultaneously tracked a total of up to ~10^7 parcels within the simulated domain. Simulations assumed $D_z = D_T(h)$, with h the height above seafloor, given by (McGinnis et al., 2014; Vielstädte et al., 2019):

$$D_T(h) = k_{Karman}\cdot u^*\cdot h \quad (7)$$

where $k_{Karman} = 0.41$ is the von Karman constant, and u^* is the shear velocity along the water current direction. u^* was calculated from ADCP data from (McGinnis et al., 2014; Vielstädte et al., 2019):

$$u^* = \frac{1}{n}\sum_{h=1}^{n}\left(\frac{u_r(h)}{ln\left(\frac{h}{h0}\right)}\right)\cdot k_{Karman} \quad (8)$$

where n is the number of ADV and ADCP bins located at ≤20 masf, $h_0 = 7.9\cdot10^{-4}$ m is the roughness length measured during the experiment (Koopmans et al., 2021), and u_r is the water current intensity.

Because ADV water current data at high acquisition rate (16 Hz) were available, the values of $D_{\parallel}$ and $D_{\perp}$could be determined from D_z based on (Berg et al., 2007):

$$D_{\parallel} = \frac{I_{\parallel}\sigma_{\parallel}^2}{I_z\sigma_z^2}D_z \quad (9)$$

$$D_{\perp} = \frac{I_{\perp}\sigma_{\perp}^2}{I_z\sigma_z^2}D_z \quad (10)$$

where I_i is the integral of the autocorrelation of the fluctuating component of the velocity in the i direction (u_i', where $u_i' = u_i - \overline{u_i}$, the difference between the instantaneous velocity and the average velocity), and σ_i^2 is the variance of u_i'. The ratios $\frac{I_{\parallel}\sigma_{\parallel}^2}{I_z\sigma_z^2}$ and $\frac{I_{\perp}\sigma_{\perp}^2}{I_z\sigma_z^2}$ were calculated based on ADV data collected during a period with water current pointing towards north. The coordinate system was double rotated to nullify mean velocities in the parallel and perpendicular directions relative to the current direction before performing the calculation.

In the model, the seafloor was assumed to have a constant depth of 119 m, considering the flat seafloor of the area, and positions were expressed as heights above the seafloor for comparison to field measurements. Tidal oscillations would slightly affect ambient pressures in the near seafloor by ≤1.5%, which was considered negligible with regards to predicted bubble dissolution and ascent trajectories. The interpolated altimeter data (Section 2.6.1) was used to determine the corresponding height above the simulated seafloor. The simulated sensor readings used a cylindrical integration cell size of 0.5 m height and 0.5 m radius. Finally, the flux of dissolved CO_2 species through the sediment-water interface was considered negligible. This assumption was supported by benthic chamber measurements performed during the CO_2 release experiment at 0.5–1.0 m from active bubble streams. No increased signal relative to background (SI Section S6) was detected during the experiment, which indicates that the flux of dissolved CO_2 across the sediment-water interface was negligible.

2.7.3. Carbonate model

The pCO_2 and the pH change was obtained for each cell by calculating the equilibrium marine carbonate system using the csys Matlab software (Zeebe and Wolf-Gladrow, 2001) (https://www.soest.hawaii.edu/oceanography/faculty/zeebe_files/CO2_System_in_Seawater/csys.html). The csys software was used to calculate the equilibrium partitioning of the carbon dioxide and related chemical species in seawater (CO_2, HCO_3^-, CO_3^{2-}), and the resulting pH (according to the total pH scale). Input parameters to the csys software included the total DIC (background DIC + simulated excess DIC), total alkalinity (2.321 mmol kg^{-1}, assumed constant and equal to the average of 46 measurements of samples taken at water depths>115 m (Martínez-Cabanas et al., 2021)), temperature, pressure, and salinity. The time-dependent background DIC was calculated from the baseline pCO_2 signal (Section 2.6.3) assuming constant total alkalinity. Csys follows Zeebe and Wolf-Gladrow (Zeebe and Wolf-Gladrow, 2001), described in detail in section S7. The kinetics of the carbonate system upon CO_2 dissolution are further discussed in Sections 3.3 and S11.

3. Results

3.1. Experimental observations

Gas bubbles were observed to exit the seafloor immediately above the injection point during the first video survey 30 min after starting the gas release. A total of up to 22 bubble stream origins were observed at the seafloor over the course of the experiment, clustered within an area of ~4 m diameter. 8 bubble streams having high to moderate flow rates were recorded from ROV videos on May 21 (after visit 3). The water column at the experimental site was well mixed between 119 and 50 m water depth and exhibited a pycnocline separating bottom from intermediate and surface water layers (Fig. 3), as further analyzed by (Esposito et al., 2021). Monitoring of about 20 h during three nights were performed at different CO_2 release flow rates (Table 1) (Schmidt, 2019). During visit 3, the Video-CTD was within 32 m of the experimental release site during 90% of the time of bottom mode operation. Visit 3 occurred at high tide (Fig. 4a,b,e), and there was an apparent inverse relationship between water current velocity (Fig. 4a) and measured pCO_2 deviations to baseline (Fig. 4c). A good agreement was found between deviations to baseline observed with pH and pCO_2 sensors, whose inlets were located at 10–20 cm distance on the Video-CTD frame. Finally, the pCH_4 sensor highlighted no deviation to baseline during visit 3. This seems to indicate that the 2.3 g d^{-1} of CH_4 injected together with the 143 kg d^{-1} of CO_2 at that point of the experiment were insufficient to enable detection of this released tracer gas in the water phase owing to the baseline level, although the large response time of this sensor may have obscured a small signal.

pCO_2 sensor 0119–001 with an inlet on the top of the Video-CTD provided readings systematically 2–3 times higher than the sensor 0412–005 attached at the bottom of the Video-CTD. Here we retained only the data from sensor 0412–005 (deployed only during visit 3). This

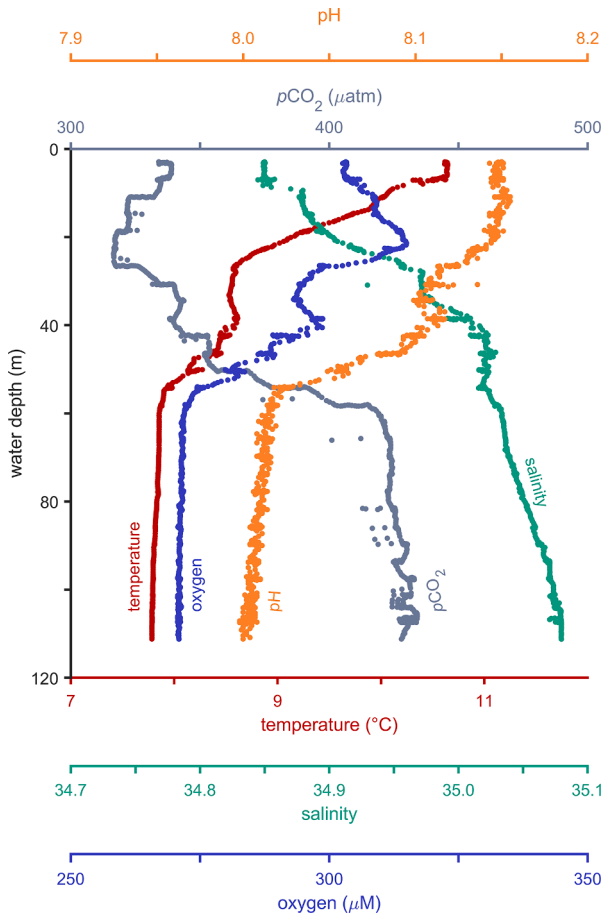

Fig. 3. Measured water-column profiles of temperature, salinity, oxygen, pCO_2, and pH at the release site (downcast for visit 3 acquired at ~110 m horizontal distance from the experimental CO_2 release site; Section 2.2).

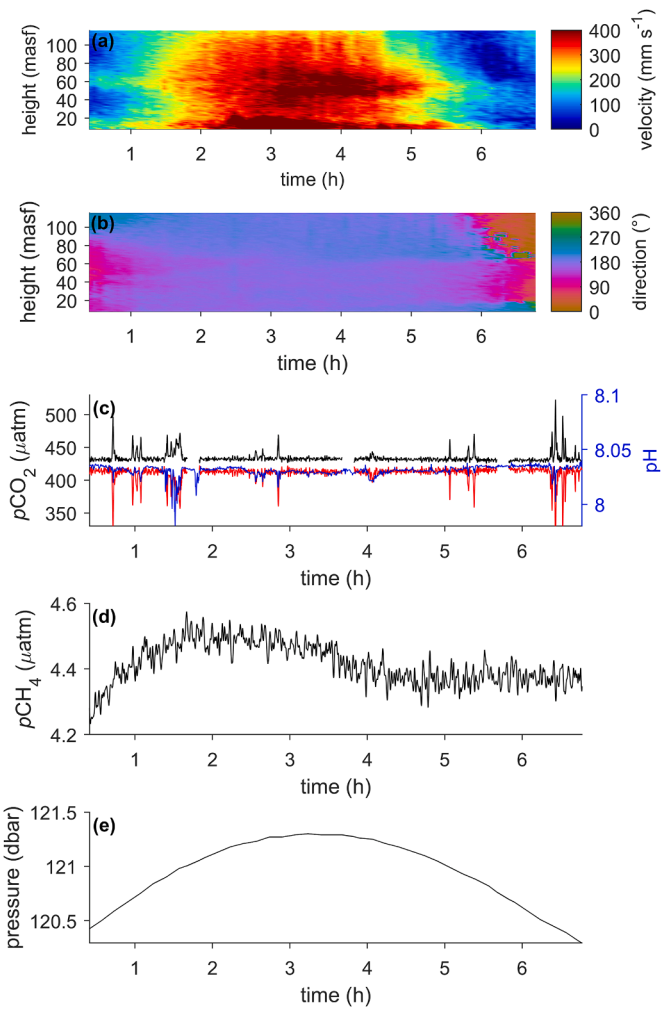

Fig. 4. Measured water current and sensor data during visit 3. (a) Water current velocity profile as a function of height above seafloor. (b) Water current direction profile as a function of height above seafloor (0° pointing towards north). (c) Instantaneous pCO_2 in bottom water (≤10 masf) based on HydroC sensor 0412–005 data (black solid line, left axis), smoothed pH sensor data in bottom water (blue solid line, right axis), and pH calculated from the pCO_2 sensor data assuming equilibrium and a constant total alkalinity of 2.321 mmol kg^{-1}* (red solid line, right axis). (d) Smoothed pCH_4 sensor data in bottom water. (e) Measured tidal pressure at the seafloor. *an offset was applied to the pH calculated from the pCO_2 sensor data (red solid line) to align it vertically with the pH sensor data.

choice was based on the fact that the presence of strong bubble plumes (i.e., including entrained seawater moving upwards (Socolofsky and Adams, 2002; Wüest et al., 1992)) were found unlikely to be able to reach >2 m above seafloor under the experimental conditions. Consequently, higher concentrations at 1.5 m additional distance from seafloor were viewed as unlikely in the field.

By use of the bubble size distribution quantification algorithm (Section 2.4), a total of 8162 bubbles were successfully detected and quantified, which were represented by 6 size bins in the simulations (Gros et al., 2019). The volume-median diameter (d_{50}) was 10.2 mm, and the observed bubble size distribution (by volume) was approximately log-normal with a standard deviation (σ) equal to 0.4 (Fig. 5a). This size distribution had a d_{50} within a factor of two of measurements performed in the North Sea above leaking wells (Vielstädte et al., 2015) and in Ardmucknish Bay, Scotland during the QICS CO_2 release experiment (Sellami et al., 2015). The total volume of the identified bubbles corresponds to a gas flow rate of 10.1 kg d^{-1} for the two sampled bubble streams, at a period during which CO_2 gas was injected at a rate of 29 kg d^{-1} into the sediment and during which additional bubble streams were observed.

The diffusion coefficients followed $D_{\parallel}(z,t) = 26 \cdot D_z(z,t)$, and $D_{\perp}(z,t) = 7.5 \cdot D_z(z,t)$, based on eqs. (9)–10. The average (0.0073 m s^{-1}) of the time-dependent u* calculated through eq. (8) from ADCP data (Figure S6) agrees well with the value of 0.0066 m s^{-1} calculated at a mean velocity of 0.11 m s^{-1} at 0.16 masf from ADV data (Koopmans et al., 2021) and the value of 0.0073 m s^{-1} calculated at steady state southbound current using an approach similar to eq. (8) with a different set of field data (Schaap et al., 2021).

3.2. *Simulated behavior of the released CO_2 gas and validation to field observations*

Based on the measured initial bubble size distribution (Sections 2.4 and 3.1, Fig. 5a), the TAMOC model simulated the changing gas bubble composition (Fig. 5b,c). Consistent with previous findings (Beaubien et al., 2014; Dewar et al., 2013; Gros et al., 2019; McGinnis et al., 2011; Schulze and Schlünder, 1985; Uchimoto et al., 2020; Vielstädte et al., 2019), we found that 99.7% of the CO_2 in the ascending bubbles dissolved within 8 m from the seafloor (Fig. 5d), and that a bubble having an initial diameter equal to the d_{50} would have decreased 10-fold in diameter when ascending to 8 masf. Since 87% of the measured bubbles had an initial diameter $<d_{50}$, the number of visible bubbles would have decreased substantially by reaching 8 masf, which agrees with the observation that bubbles (>1 mm in diameter (Dewar et al., 2021) were not visible on the ROV videos at >8 masf (Flohr et al., 2021a). This finding is further supported by the increase in methane content and in $\delta^{13}C$ of CO_2 of the gas bubbles with height above seafloor due to

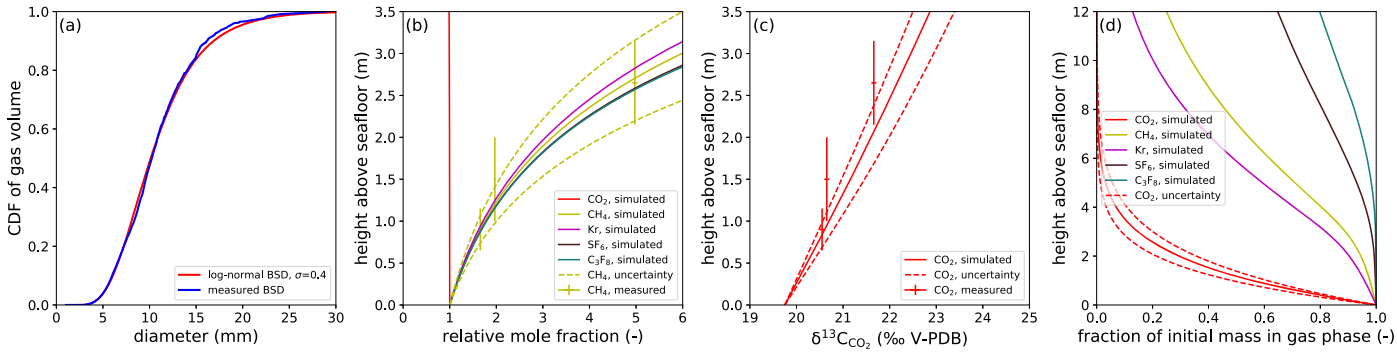

Fig. 5. (a) Measured initial bubble size distribution (BSD) expressed as the cumulative density function (CDF) of gas volume, blue solid line, which corresponds closely to a log-normal distribution with σ = 0.4, red solid line. (b) Simulated increase in relative mole fraction (mole fraction normalized to the initial mole fraction) within 0–3.5 masf for key simulated gases, compared to values measured for CH_4 on collected samples of bubble gas. The bubble gas samples were collected at different heights above seafloor with a ROV during separate dives on May 19 and 21, 2019, and the sizes of the horizontal and vertical bars indicate the uncertainty in measured composition and vertical height of sample collection, respectively. The uncertainty bounds on the simulated curves (dashed lines, shown for CH_4 on panel b and for CO_2 on panels c and d) were obtained by assuming a ± 20% uncertainty on the initial BSD. (c) Simulated increase in $\delta^{13}C$ within 0–3.5 masf for CO_2, compared to values measured on collected samples of bubble gas; $\delta^{13}C$ values are expressed relative to the Vienna Pee Dee Belemnite (V-PDB). (d) Fraction of the initially-released mass of gases at the seafloor remaining in gas phase within 0–12 masf.

preferential dissolution of the CO_2, as measured in the laboratory from collected gas samples (Section 2.5), which corroborates the simulated evolution of the bubble gas composition (Fig. 5b,c).

The shape of the simulated plume is largely driven by advection due to the strong water currents at the experimental site (average 0.15 m s^{-1} at 3.2–5.2 masf over the ADCP deployment), and a typical simulated situation is shown in Fig. 6. Consequently, turbulent mixing generates only limited horizontal and vertical movements of the DIC in the simulated domain (Fig. 7). Hence, the plume remained relatively narrow according to the simulations (<15 m width at 10–20 m downstream of the source for a typical situation, Fig. 7b).

A simulation for CH_4 (section S9) predicted a maximum additional concentration of CH_4 arising from the experimental release of $1.6{\cdot}10^{-8}$ kg m^{-3} for the simulated pCH_4 sensor trajectory, which is 13% of the background CH_4 concentration observed within the bottom water column (≤10 masf) (Fig. 4d), and 60% of the noise in instantaneous pCH_4 sensor data. The maximum simulated additional concentration of Kr arising from the experimental release is $3.0{\cdot}10^{-8}$ kg m^{-3} for the simulated Video-CTD trajectory, which is smaller than the background concentration of $2.8{\cdot}10^{-7}$ kg m^{-3}, assuming equilibrium with the atmosphere. CH_4 and Kr are less soluble than CO_2, with peak input to the water column at 4.7 and 4.3 masf, respectively.

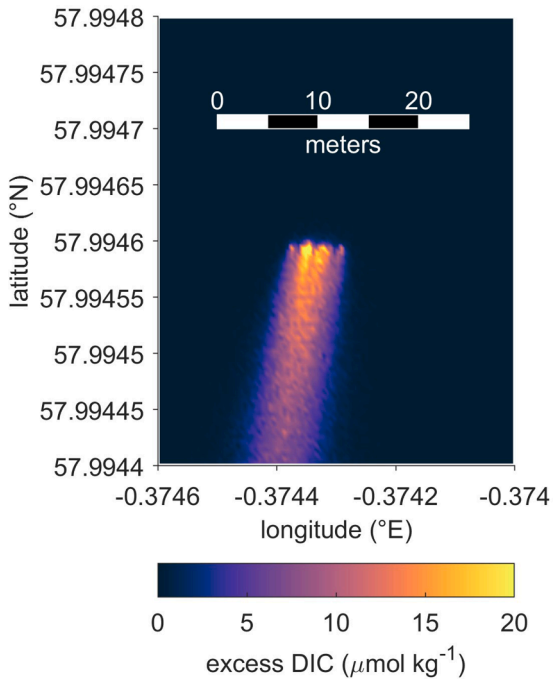

Fig. 6. Typical simulated plume shape during a period with almost constant, approximately southwards tidal current (00:30 on May 20, during visit 3), shown for excess DIC, calculated at 0–1 masf. A hundred cells were used in each direction, having 45 cm and 35 cm in the latitudinal and longitudinal directions, respectively.

3.3. *Estimated release flow rate from field data and model simulations*

The predicted flow rate of CO_2 leakage at the seafloor was 91 kg d^{-1} for visit 3, or 36% lower than the known flow rate injected into the sediment (143 kg d^{-1}). As explained in Section 2.7, these estimated flow rates were derived by minimizing the difference between measurements of pCO_2 performed in the field (with a towed sensor) and the simulated readings. Overall, the presence of a deviation from the baseline signal in the field measurements usually corresponded to the presence of a simulated deviation from baseline signal (Fig. 8), with a correlation coefficient between the measured pCO_2 and the corresponding simulated values of 0.28. This indicates that the simulated positions of the towed sensor closely reproduced the actual positions of the sensor during the deployment. This suggestion is supported in examining the similarity of the observed and simulated signals in three dimensions (Fig. 9). The peak heights were not reproduced exactly by the model, which is in part due to the difficulties of identifying accurate positions of the sensor towed during the experiment and contribution from kinetics of the carbonate system. The narrowness and very limited height of the elevated signal also contribute.

A simplified sensitivity analysis was conducted (Table S3) to explore the contributions of some key controlling parameters. The choice of the D_x, D_y, and D_z values is often difficult to make, and uncertainty arises from a variety of existing formulations (Holtappels and Lorke, 2011; McGinnis et al., 2014; Rovelli et al., 2016) and from insufficient availability of field data to precisely constrain these parameters. In the vicinity of the lower boundary of water bodies, which is the main region of interest for CO_2 leakage, D_z is usually considered to depend on the height above the bottom sediment (McGinnis et al., 2014; Vielstädte et al., 2019; Wüest et al., 2000). However, for convenience or due to lack of available field data, a single value is sometimes assumed for the whole water column or two separate values for the water column center and the boundary regions (Dissanayake et al., 2012; French McCay et al., 2015). Different methods can lead to predictions of $D_{\parallel}$, $D_{\perp}$ (or sometime

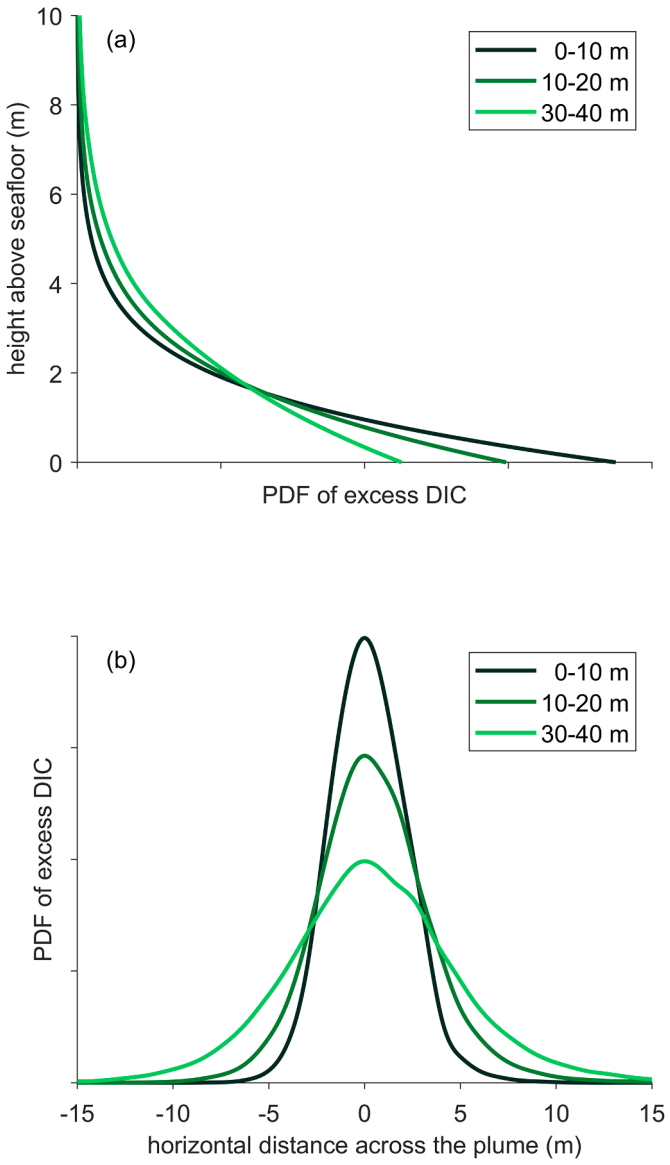

Fig. 7. (a) Simulated probability density function (PDF) of excess DIC in vertical direction at 0–10, 10–20, and 30–40 m horizontal distance from the gas sources. (b) Simulated PDF of excess DIC in horizontal direction across the plume at 0–10, 10–20, and 30–40 m horizontal distance from the gas sources. Values calculated at 00:30 on May 20, during visit 3.

D_x, D_y), and D_z differing by an order of magnitude or more (Dissanayake et al., 2012; Holtappels and Lorke, 2011). Moreover, D_x and D_y are dependent on the horizontal scale considered because the range of size of the eddies contributing to diffusion increases with increasing horizontal scale (Fischer et al., 1979; Okubo, 1972). When the selected diffusion coefficient values are decreased or increased by an order of magnitude, or if their value is assumed independent of height above seafloor, predicted CO_2 leak flow rates vary by up to 53% relative to the best estimate (Table S3).

The initial bubble size distribution is also a key driver that controls the speed of ascent of gas bubbles and the rate of mass transfer of chemicals across the bubble-seawater interface (Cooper et al., 2021; Dewar et al., 2015; Gros et al., 2017; Leifer, 2019; McGinnis et al., 2011, 2006; Olsen et al., 2019; Olsen et al., 2017; Socolofsky and Gros, 2019). Bubble size distribution determination usually relies on custom-built instruments and software. Using a d_{50} of 2.5 or 20.4 mm, i.e. the approximate minimum and maximum d_{50} values reported in the literature, instead of the simulated d_{50}, increases the estimated CO_2 gas flow rate exiting the seafloor by 103% and 11%, respectively, for visit 3. A smaller discrepancy (27%) with the simulation using the measured initial bubble size distribution is found when the d_{50} is taken as twice the minimum value reported in the literature (5.1 mm or half of the d_{50} value observed during the experiment).

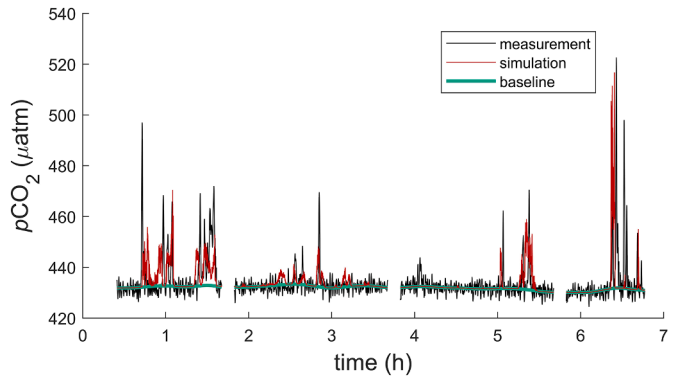

Fig. 8. Measured, simulated, and baseline pCO_2 signal during visit 3. Simulation assumed the best-fit flow rate of 91 kg d^{-1} exiting the seafloor for visit 3. The estimated baseline (green solid line) was calculated for visit 3 based on the method of Eilers (Eilers, 2004), as described in Section 2.6.3 (the baseline pCO_2 was assumed homogeneous within the near-seafloor bottom water mass). The estimated baseline was used in the simulations, where predicted pCO_2 levels are determined by combining the space- and time-dependent simulated DIC excess originating from the release with the time-dependent background baseline CO_2 level, using the csys software (Section 2.7.3).

The simulated trajectory of the pCO_2 sensor also exerts an important control on the estimated gas flow rate out of the sediment. Three major potential contributions to the existing uncertainty in the simulated sensor positions were assumed: (a) a possible small, systematic error on the position of the point of entry of the Video-CTD at the sea surface, (b) uncertainty of the horizontal displacement of the instrument close to the seafloor level relative to the point of entry in seawater, (c) limited precision of the GPS antenna on the research vessel. Unfortunately, only systematic errors (a) can be investigated easily in a sensitivity analysis. A systematic change of just 1 m in position along or perpendicular to the axis of the research vessel leads to predicted flow rates spanning from, respectively, −3 to +2% and −11 to +17% of the best-estimate CO_2 leakage rate.

Uncertainty in the carbonate system affects the estimated leakage flow rate. Error propagation within the carbonate system (Orr et al., 2018) indicated that the pCO_2 uncertainty for calculation from DIC and total alkalinity for concentrations close to baseline (pCO_2 = 420 μatm, DIC = 2.161 mmol kg^{-1}, total alkalinity = 2.321 mmol kg^{-1}) would amount to 50 μatm (12%), driven at 95% by the large uncertainty of the total alkalinity (two standard deviations from 46 hourly measurements: 20.2 μmol kg^{-1}). However, the estimated flow rate is based on the difference between a simulated elevated pCO_2 signal (calculated from baseline derived from field measurements and from simulated deviation) to a measured pCO_2 background. Consequently, error contributions are limited to periods with simulated deviations from baseline, and will scale with the magnitude of the deviation to the baseline. In the sensitivity analysis, the dominant effect of total alkalinity on the estimated flow rate was evaluated for (a) using a constant total alkalinity assumed equal to the measured average alkalinity minus two standard deviations, (b) using a constant total alkalinity assumed equal to the measured average alkalinity plus two standard deviations, and (c) using a total alkalinity drawn at each time step from a normal distribution having mean and standard deviation as observed from measurements of discrete water samples. These scenarios lead to a change in the estimated flow rate at the seafloor of a maximum of ±1%.

Additionally, the kinetics of hydration and hydroxylation of CO_2 to HCO_3^- were evaluated to be relatively slow in cold bottom water with a

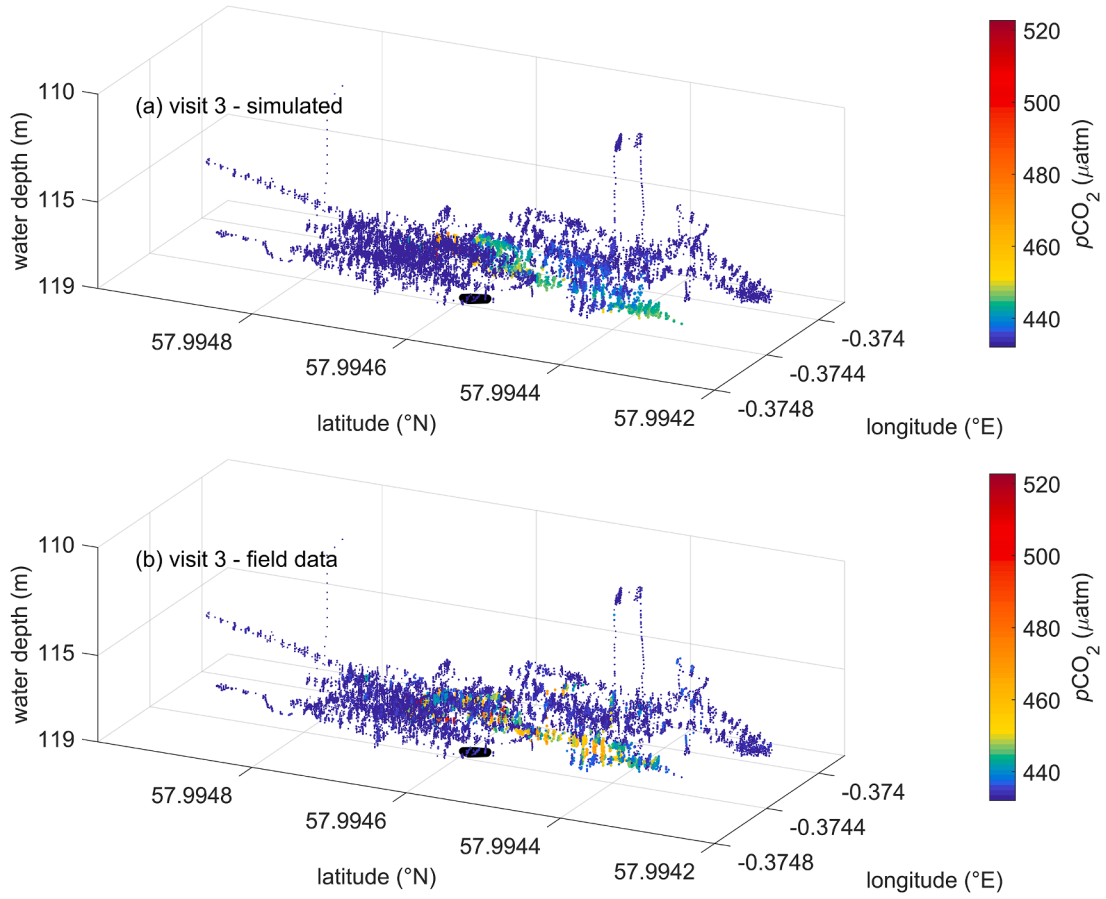

Fig. 9. Comparison of simulated and measured spatial distribution of pCO_2 during visit 3. The dots represent values at the time when the towed pCO_2 sensor was at the corresponding location, and dot diameter is proportional to the measured or simulated pCO_2 value. The black shape indicates the observed location of the bubble streams.

calculated 63% equilibration time for the conditions of the experiment of ~117.5 s (section S11, Koopmans et al., 2021). These kinetics could therefore have affected the sensor readings, owing to the average duration between contact of water with dissolving bubbles and pCO_2 sensor measurement for non-baseline pCO_2 sensor signal that was 111 s and the sensor response time of 140 s. This process would have led to pCO2 larger and pH lower than equilibrium values within the monitored seawater (section S11), and could therefore have affected the estimated leakage flow rate.

3.4. Estimated limit of detection

A limit of detection for a gaseous CO_2 release can be estimated for the specific setting and deployment conditions, based on field measurements. Based on the size of the third largest measured pCO_2 peak, the estimated limit of detection was ~15 kg d^{-1}, assuming that the limit of detection is reached when the signal-to-noise ratio equals 3. This is coherent with the absence of detection of any peak during visit 1 (release flow rate of 6 kg d^{-1}) with the pCO_2 sensor 0119–001 (Martínez-Cabanas et al., 2021).

4. Discussion

4.1. Tracers and trace gases as a means to detect dissolution of CO_2 from gas bubbles

The use of tracer gases is not prerequisite for leakage flow rate quantification of CO_2 (Section 3.3), but is a key tool to validate CO_2 dissolution simulations (Section 3.2) and for leakage attribution (Flohr et al., 2021b). Fig. 5b,c further highlights the importance of tracer gases (Roberts et al., 2017) and carbon isotopes to detect dissolution of a high-purity CO_2 gas. Whereas 90% of the released CO_2 gas aqueously dissolved by 3.5 masf according to the simulation (Fig. 5d), the simulated CO_2 mole fraction in the bubble gas decreased only from 99.99% to 98.61% (Fig. 5b). Such a difference cannot be monitored with the selected analytical technology, because a mole fraction close to 100% is difficult to precisely determine analytically. The increase of the mole fraction of CH_4 caused by preferential dissolution of CO_2 is measurable, and the overall tracer mole fraction was predicted to have increased from 0.01% to 0.08% by 3.5 masf, with the remaining 1.31% constituted by atmospheric gases (O_2, N_2, and Ar) stripped from the ambient seawater. Such trace mole fractions can be determined analytically, and such increases (e.g., 8× from 0.01% to 0.08% for tracer gases or 0.00% to 1.31% for atmospheric gases) are easily monitored, and therefore enable detection of CO_2 dissolution. The ^{13}C isotope content of the CO_2 also detected the CO_2 dissolution, similar to an approach that has been used for CH_4 at a natural seep (Leonte et al., 2018). As an alternative approach to the one chosen here, atmospheric gases can be used to monitor CO_2 dissolution (Beaubien et al., 2014).

For measurement of tracers in aqueous phase, the in-situ pCH_4 sensor measurements (Fig. 4d) did not detect any deviation from baseline signal in relation with the experimental release. This finding is confirmed by simulations indicating predicted additional concentrations arising from the experimental release were ≤60% of the noise level of the pCH_4 sensor (Section 3.2). The predicted effect of experimentally-released Kr on the bottom-water Kr concentration is ≤11% of the background concentration. Consequently, for the experimental conditions investigated here, in situ sensor monitoring of dissolved CO_2 rather

than dissolved tracers enabled leakage detection and quantification from the aqueous phase.

4.2. Fitness of the approach for leakage detection and quantification

The CO_2 leakage flow rate at the seafloor predicted for visit 3 is 91 kg d^{-1}, which is 36% lower than the known flow rate injected into the sediment (143 kg d^{-1}). This indicates that 36% of the injected CO_2 was retained in the sediment, either as dissolved CO_2 within the seafloor or temporarily as gas pockets (Flohr et al., 2021b; Roche et al., 2021). This finding is consistent with estimates that 41% of the injected CO_2 dissolved within the sediment (Flohr et al., 2021b), and represents a slightly higher leakage flow rate estimate at the seafloor than the range of 55–69 kg d^{-1} determined by extrapolation from measurements of the volume flow rates of individual bubble streams (Flohr et al., 2021b). Similarly, the current estimate (64% of injected CO_2 emerging at the seafloor) lies within the range of reported leakage estimates of 22–62% derived via passive acoustics (Li et al., 2021) and of 73±13% determined by eddy covariance (Koopmans et al., 2021) at the highest injection flow rate of 143 kg d^{-1}.

The proposed method provides a quantification of the overall flow rate for several active CO_2 seeps at the seafloor. This estimate is based on an indirect and non-invasive method, enabling quantification of the aggregated flow rate of several point sources. The method also provides on-line monitoring of the pCO_2 signal as well as video monitoring of the seafloor immediately below the instrument, and the operator can therefore evaluate in real time the collected field data and adapt the deployment strategy accordingly. The method also has potential for site monitoring and leakage detection, owing to the real-time data readings on-board the vessel. Because the simulated plumes were very narrow (Figs. 6 and 7b) and had limited vertical extension into the higher water column (Fig. 7a), monitoring strategies should consider deployment of towed sensors as close as technically possible to the seafloor.

The estimated limit of detection of ~15 kg d^{-1} for the deployment conditions (Section 3.4) highlights that the method is capable of detecting and quantifying leaks well below the suggested regulatory limit of 1% reservoir loss in 100 years, even for small reservoirs (10 Mt) for which this limit corresponds to 2700 kg d^{-1} (Dean et al., 2020). The limit of detection could be further improved by e.g., slower towing speed of sensors in the vicinity of the emission source, measurements at weaker water currents or during slack tide, and deployment of the sensors as close as possible to the seafloor at calm sea state. Additionally, a more controlled and accurate positioning of the sensors would enable improved monitoring.

The selected numerical modeling approach is based on measured water currents, and therefore does not require implementation of a complex hydrodynamic model as used in other simulations (e.g., Blackford et al., 2020). Such hydrodynamic models require high computational power and simulation times usually count in weeks on dedicated computational servers (depending on selected precision and period of time simulated). To the contrary, the simulations reported here could be performed on a 16 GB RAM laptop, making the simulation tool portable and easy to use (possibly even at sea). This type of approach may be favored for industrial or governmental leakage monitoring and early warning applications, as access to computational clusters may be limited on offshore installations and vessels. However, the non-negligible kinetics of the carbonate system at near-bottom seawater temperatures (frequently <10 °C across the globe) pose a further complication for future application of the method for leakage quantification.

Gas-phase (bubble) leakage at the seafloor as investigated with the present approach may not happen immediately upon CO_2 escape from the geologic reservoir, typically located hundreds to thousands of meters below the seafloor. Depending on leakage pathways (e.g., blowout, borehole leakage, caprock failure), a wide variety of behaviors may be expected (IPCC, 2005). The high solubility of CO_2 can lead to rapid dissolution, such that a leakage sourced deep into the underground may initially not have a manifestation at the seafloor, though seismic measurement techniques could be used to monitor storage integrity (IPCC, 2005). Such an underground leakage could drive a migration of formation brine (IPCC, 2005) and chemical fractionation and mixing within reservoirs and during upward migration (Anderson et al., 2019; Weber et al., 2021). Several natural processes may act to delay or prevent upward migration, such as the increased density of CO_2-laden brines (IPCC, 2005). During the CO_2 release experiment, pore water analysis combined with simulations highlighted various increases in pore water metal ion content and a temperature increase, controlled by carbonate and silicate mineral dissolution resulting from CO_2 dissolution into pore water (Lichtschlag et al., 2021). Model simulations predicted an upward pore water movement at 0.3 m d^{-1} during the experiment (Lichtschlag et al., 2021). It remains unclear to what extent and over which time window such precursor indicators could be observed within the shallow seafloor before gas bubble arrival. However, it is likely that upon gas breakthrough a major fraction of the CO_2 escaping from the seafloor would be in gas form as observed during the current experiment as well as at the Panarea natural seep site (Molari et al., 2018).

4.3. Leakage quantification sensitivity to input data

For quantification of a potential CO_2 leak, several parameters must be measured in the field when using the described combined approach. A pCO_2 (or pH) sensor is towed in the vicinity of a postulated leakage area, in close vicinity to the seafloor. The choice of the measured parameter (pCO_2 or pH) is theoretically equivalent as one can be calculated from the other based on measured total alkalinity, if equilibrium can be assumed. However, because equilibrium of the carbonate system is likely not to be fully achieved in the immediate vicinity of dissolving CO_2 bubbles, pCO_2 measurement has a theoretical advantage over pH for leakage detection (Figures S7 and S8). For the current experiment, the pCO_2 sensor data was selected because these data had a larger signal-to-noise ratio compared to the pH sensor data. Position of bubble stream origins must also be determined relative to the sensor measurements. For the narrow plumes (<15 m width at 10–20 m downstream from source) simulated for the CO_2 release experiment where sources were clustered within a 2-m diameter area, the estimated ±2.5 m uncertainty on positions was sufficient to enable a leakage quantification in agreement with estimates from other methods (Section 4.2). However, deeply sourced leaks–such as from targeted CO_2 storage reservoirs–might be expected to cover larger surface areas at the seafloor than the one observed during the experiment. The maximum distance observed here between the bubble stream origins (~4 m) for a CO_2 source at 3 m below the seabed was smaller than the maximum distance between the bubble stream origins (~13 m, Dewar et al., 2015) observed for the QICS experiment, where the CO_2 injection point was located deeper at 10 m below the seabed. Measured water current profiles were used to drive advection in the model, and are therefore a necessary input at least for the lower part of the water column affected by the leaked CO_2; the ADCP data used here had a sampling rate of 0.2 min^{-1}, which was sufficient for driving the advection model.

The initial bubble size distribution must also be measured immediately above the seafloor (<1 masf). Initial bubble size distributions in the marine environment vary depending on local settings, with diameters spanning from approximately 2 to 25 mm and d_{50} values usually in the range 3–20 mm (Gros et al., 2019; Römer et al., 2012; Sellami et al., 2015; Vielstädte et al., 2015; Wang and Socolofsky, 2015). Factors controlling the size of bubbles exiting from natural seafloors are poorly known (Liu, 2019), but may include parameters such as sediment grain size (Delwiche and Hemond, 2017; Leifer, 2019; Leifer and Culling, 2010; Liu et al., 2018; Liu et al., 2016). Recently-reported field observations indicate that initial bubble size can vary with time at a single site, and that a dependence on gas flow rate might exist (Delwiche and

Hemond, 2017; Razaz et al., 2020). The determination of accurate bubble size distribution requires advanced systems involving two cameras for stereo imaging (Wang and Socolofsky, 2015), though satisfactory results can frequently be obtained with systems involving a single camera such as in the current study (Li et al., 2021). The estimated flow rate showed high sensitivity (up to 103% increase of the estimated leakage flow rate exiting the seafloor) to the initial bubble size distribution, when varied over the range of existing observations worldwide (Gros et al., 2019; Vielstädte et al., 2015; Wang and Socolofsky, 2015). Among the data used for leakage rate quantification, (apart from gas composition) the initial bubble size distribution is the only parameter that required ROV instrument deployment, which can represent a major added cost. Models to estimate bubble sizes from conditions at the gas release orifice only exist for releases from jets and plumes exiting from circular orifices (Wang et al., 2018) such as leaking or severed pipes. However, in order to enable a purely ship-based monitoring and initial leakage rate estimate, the bubble size distribution might be estimated by fitting the size distribution to the observed flare height recorded with ship-based active acoustic instruments (e.g., EK60) by assuming a reasonable composition of the leaking gas, such as has been done for natural gas seeps (Jun, 2018; Wang et al., 2020). Further techniques might be envisioned to estimate bubble size. For example, active acoustics are able to identify the size of individual bubbles (Lohrberg et al., 2020), but have difficulties measuring the sizes of multiple bubbles emitted at short time interval (Lohrberg et al., 2020; Veloso et al., 2015), which limits the range of applicability of the method. Optical sensors (Delwiche and Hemond, 2017) or a scale visible on the HD video might be mounted on the Video-CTD, however such techniques require a sufficient time spent directly above the bubble streams (optical sensor) or acceptable angle of view and sufficient time spent with the scale within the bubble streams (scale on HD video). Such conditions may be difficult to ensure from a towed platform depending on sea conditions.

Additionally, basic oceanographic parameters must also be monitored (salinity, temperature, total alkalinity, and dissolved oxygen concentration), as they partly control bubble dissolution. Finally, gas bubble composition measurement may be advisable to ascertain the simulated initial gas composition and to determine the source of the released gas (Flohr et al., 2021b).

The 7 h deployment time for the towed sensor during visit 3 proved sufficient for leakage rate quantification. In general, longer deployment times enable better constraints of leakage rate, and monitoring over one to several tidal cycles might be advisable as tidal fluctuations have been shown to affect gas emission rates at natural seep sites (Blackford et al., 2014; Boles et al., 2001; Martens and Val Klump, 1984; Römer et al., 2016; Torres et al., 2002). Tidal currents also tend to dilute the emitted DIC such that elevated *p*CO2 signals were more prominent at lower water currents (Fig. 4a,c).

5. Conclusion

Simulations and field sampling were combined to provide an effective strategy for quantification of CO_2 leakage into the marine environment. This is a new paradigm in the field of CO_2 leakage monitoring, where simulations have, until now, remained largely disconnected from direct field applications, and mostly used to investigate leakage scenarios or to provide an overall understanding of inherently patchy field data. Our combined approach relies on pCO_2 data measured by a towed sensor within the bottom water close to the CO_2 release site. Here, the validity of the method was demonstrated for a relatively small-scale release with eight identified bubble streams originating over a small seafloor footprint. The estimated CO_2 leakage rate agrees with published estimates obtained with other methods. Our approach can be applied over much larger areas of CO_2 leakage (Gros et al., 2019). For numerous distributed sources of CO_2 emissions from the seafloor, concentration measurements in the aqueous phase may be the only practical approach for quantifying CO_2 emission from CCS sites.

Declaration of Competing Interest

The authors declare that they have no known competing financial interests or personal relationships that could have appeared to influence the work reported in this paper.

Acknowledgments

We thank the captains and crews for support provided during the *RV Poseidon* and *RRS James Cook* cruises, the ROV Isis team, Sergiy Cherednichenko and Andrea Bodenbinder for technical support aboard *RV Poseidon*, Isabelle Mekelnburg for support aboard *RRS James Cook*, and Karen Hissmann, Reimar Wolf, and Nadja Kinski for discussions. We additionally thank the three anonymous reviewers for their suggestions. This project has received funding from the European Union's Horizon 2020 research and innovation program under grant agreement No. 654462 STEMM-CCS.

Supplementary materials

Supplementary material associated with this article can be found, in the online version, at doi:10.1016/j.ijggc.2021.103387.

Appendix

The Appendix document contains: S1 correlation of water currents at 0.16 and 3.2 masf during the CO_2 release experiment; S2 data processing procedure for the altimeter data; S3 fitting of coefficient in equation 1; S4 baseline pCO_2 during visit 3; S5 chemical properties of the simulated molecules; S6 benthic chamber deployments performed during the release experiment; S7 detailed description of the csys carbonate model; S8 shear velocity calculated from ADCP data; S9 assumptions made for the CH_4 and Kr simulations; S10 sensitivity analysis; S11 discussion of the carbonate system kinetics.

References

Anderson, J., Romanak, K., Alfi, M., Hovorka, S., 2019. Light hydrocarbon and noble gas migration as an analogue for potential CO_2 leakage: numerical simulations and field data from three hydrocarbon systems. Greenh. Gases Sci. Technol. 9, 226–244. https://doi.org/10.1002/ghg.1841.

Atamanchuk, D., Tengberg, A., Aleynik, D., Fietzek, P., Shitashima, K., Lichtschlag, A., Hall, P.O.J., Stahl, H., 2015. Detection of CO_2 leakage from a simulated sub-seabed storage site using three different types of pCO_2 sensors. Int. J. Greenh. Gas Control, CCS Marine Environ. 38, 121–134. https://doi.org/10.1016/j.ijggc.2014.10.021.

Beaubien, S.E., De Vittor, C., McGinnis, D.F., Bigi, S., Comici, C., Ingrosso, G., Lombardi, S., Ruggiero, L., 2014. Preliminary experiments and modelling of the fate of CO_2 bubbles in the water column near Panarea Island (Italy). Energy Procedia 59, 397–403. https://doi.org/10.1016/j.egypro.2014.10.394.

Berg, P., Røy, H., Wiberg, P.L., 2007. Eddy correlation flux measurements: the sediment surface area that contributes to the flux. Limnol. Oceanogr. 52, 1672–1684. https://doi.org/10.4319/lo.2007.52.4.1672.

Blackford, J., Alendal, G., Avlesen, H., Brereton, A., Cazenave, P.W., Chen, B., Dewar, M., Holt, J., Phelps, J., 2020. Impact and detectability of hypothetical CCS offshore seep scenarios as an aid to storage assurance and risk assessment. Int. J. Greenh. Gas Control 95, 102949. https://doi.org/10.1016/j.ijggc.2019.102949.

Blackford, J., Artioli, Y., Clark, J., de Mora, L., 2017. Monitoring of offshore geological carbon storage integrity: implications of natural variability in the marine system and the assessment of anomaly detection criteria. Int. J. Greenh. Gas Control 64, 99–112. https://doi.org/10.1016/j.ijggc.2017.06.020.

Blackford, J., Stahl, H., Bull, J.M., Bergès, B.J.P., Cevatoglu, M., Lichtschlag, A., Connelly, D., James, R.H., Kita, J., Long, D., Naylor, M., Shitashima, K., Smith, D., Taylor, P., Wright, I., Akhurst, M., Chen, B., Gernon, T.M., Hauton, C., Hayashi, M., Kaieda, H., Leighton, T.G., Sato, T., Sayer, M.D.J., Suzumura, M., Tait, K., Vardy, M. E., White, P.R., Widdicombe, S., 2014. Detection and impacts of leakage from sub-seafloor deep geological carbon dioxide storage. Nat. Clim. Change 4, 1011–1016. https://doi.org/10.1038/nclimate2381.

Blackford, J., Stahl, H., Kita, J., Sato, T., 2015. CCS and the marine environment. Int. J. Greenh. Gas Control 1–230.

Blackford, J.C., Torres, R., Cazanave, P., Artioli, Y., 2013. Modelling dispersion of CO_2 plumes in sea water as an aid to monitoring and understanding ecological impact. In: Energy Procedia, GHGT-11 Proceedings of the 11th International Conference on Greenhouse Gas Control Technologies, 37, pp. 3379–3386. https://doi.org/10.1016/j.egypro.2013.06.226, 18-22 November 2012, Kyoto, Japan.

Boles, J.R., Clark, J.F., Leifer, I., Washburn, L., 2001. Temporal variation in natural methane seep rate due to tides, Coal Oil Point area, California. J. Geophys. Res. Oceans 106, 27077–27086. https://doi.org/10.1029/2000JC000774.

Clift, R., Grace, J.R., Weber, M.E., 1978. Bubbles, Drops, and Particles. Academic Press, New York.

Connelly, D., et al., 2009. RRS James Cook Cruise JC108 25 April –30 May 2019. Strategies for the Environmental Monitoring of Marine Carbon Capture and Storage, STEMM-CCS (National Oceanography Centre Cruise Report No. 63). National Oceanography Centre, Southampton, UK.

Cooper, C., Adams, E., Gros, J., 2021. An evaluation of models that estimate droplet size from subsurface oil releases. Mar. Pollut. Bull. 163, 111932 https://doi.org/10.1016/j.marpolbul.2020.111932.

Dale, A.W., Sommer, S., Lichtschlag, A., Koopmans, D., Haeckel, M., Kossel, E., Deusner, C., Linke, P., Scholten, J., Wallmann, K., van Erk, M., Gros, J., Scholz, F., Schmidt, M., 2021. Defining a biogeochemical baseline for sediments at Carbon Capture and Storage (CCS) sites: an example from the North Sea (Goldeneye). Int. J. Greenh. Gas Control 106, 103265. https://doi.org/10.1016/j.ijggc.2021.103265.

Dean, M., Blackford, J., Connelly, D., Hines, R., 2020. Insights and guidance for offshore CO_2 storage monitoring based on the QICS, ETI MMV, and STEMM-CCS projects. Int. J. Greenh. Gas Control 100, 103120. https://doi.org/10.1016/j.ijggc.2020.103120.

Delwiche, K.B., Hemond, H.F., 2017. Methane bubble size distributions, flux, and dissolution in a freshwater lake. Environ. Sci. Technol. 51, 13733–13739. https://doi.org/10.1021/acs.est.7b04243.

Dewar, M., Saleem, U., Flohr, A., Schaap, A., Strong, J., Li, J., Roche, B., Bull, J.M., Chen, B., Blackford, J.C., 2021. Analysis of the physicochemical detectability and impacts of offshore CO_2 leakage through multi-scale modelling of in-situ experimental data using the PLUME model. Int. J. Greenhouse Gas Control (in the Special Issue on STEMM-CCS).

Dewar, M., Sellami, N., Chen, B., 2015. Dynamics of rising CO_2 bubble plumes in the QICS field experiment: part 2 – Modelling. Int. J. Greenh. Gas Control 38, 52–63. https://doi.org/10.1016/j.ijggc.2014.11.003.

Dewar, M., Wei, W., McNeil, D., Chen, B., 2013. Small-scale modelling of the physiochemical impacts of CO_2 leaked from sub-seabed reservoirs or pipelines within the North Sea and surrounding waters. Mar. Pollut. Bull., Ecological Impacts CCS Leakage 73, 504–515. https://doi.org/10.1016/j.marpolbul.2013.03.005.

Dissanayake, A.L., DeGraff, J.A., Yapa, P.D., Nakata, K., Ishihara, Y., Yabe, I., 2012. Modeling the impact of CO_2 releases in Kagoshima Bay. Japan. J. Hydro-Environ. Res. 6, 195–208. https://doi.org/10.1016/j.jher.2012.02.001.

Dissanayake, A.L., Gros, J., Socolofsky, S.A., 2018. Integral models for bubble, droplet, and multiphase plume dynamics in stratification and crossflow. Environ. Fluid Mech. 18, 1167–1202. https://doi.org/10.1007/s10652-018-9591-y.

Dixon, T., Romanak, K.D., 2015. Improving monitoring protocols for CO_2 geological storage with technical advances in CO_2 attribution monitoring. Int. J. Greenh. Gas Control 41, 29–40. https://doi.org/10.1016/j.ijggc.2015.05.029.

Eilers, P.H.C., 2004. Parametric time warping. Anal. Chem. 76, 404–411. https://doi.org/10.1021/ac034800e.

Esposito, M., Martínez-Cabanas, M., Connelly, D.P., Jasinski, D., Linke, P., Schmidt, M., Achterberg, E.P., 2021. Water column baseline assessment for offshore carbon dioxide capture and storage (CCS) sites: analysis of field data from the Goldeneye storage complex area. Int. J. Greenh. Gas Control 109, 103344. https://doi.org/10.1016/j.ijggc.2021.103344.

EU GeoCapacity, 2009. D16, WP2 report, Storage capacity. Assessing European Capacity For the Geological Storage of Carbon Dioxide.

Fischer, H.B., List, E.J., Koh, R.C.Y., Imberger, J., Brooks, N.H., 1979. Mixing in Inland and Coastal Waters. Academic Press, London.

Flohr, A., Schaap, A., Achterberg, E.P., Alendal, G., Arundell, M., Berndt, C., Blackford, J., Böttner, C., Borisov, S.M., Brown, R., Bull, J.M., Carter, L., Chen, B., Dale, A.W., de Beer, D., Dean, M., Deusner, C., Dewar, M., Durden, J.M., Elsen, S., Esposito, M., Faggetter, M., Fischer, J.P., Gana, A., Gros, J., Haeckel, M., Hanz, R., Holtappels, M., Hosking, B., Huvenne, V.A.I., James, R.H., Koopmans, D., Kossel, E., Leighton, T.G., Li, J., Lichtschlag, A., Linke, P., Loucaides, S., Martínez-Cabanas, M., Matter, J.M., Mesher, T., Monk, S., Mowlem, M., Oleynik, A., Papadimitriou, S., Paxton, D., Pearce, C.R., Peel, K., Roche, B., Ruhl, H.A., Saleem, U., Sands, C., Saw, K., Schmidt, M., Sommer, S., Strong, J.A., Triest, J., Ungerböck, B., Walk, J., White, P., Widdicombe, S., Wilson, R.E., Wright, H., Wyatt, J., Connelly, D., 2021a. Towards improved monitoring of offshore carbon storage: a real-world field experiment detecting a controlled sub-seafloor CO_2 release. Int. J. Greenh. Gas Control 106, 103237. https://doi.org/10.1016/j.ijggc.2020.103237.

Flohr, A., Matter, J.M., James, R.H., Saw, K., Brown, R., Gros, J., Flude, S., Day, C., Peel, K., Connelly, D., Pearce, C.R., Strong, J., Lichtschlag, A., Hillegonds, D.J., Ballentine, C.J., Tyne, R.L., 2021b. Utility of natural and artificial geochemical tracers for leakage monitoring and quantification during an offshore controlled CO_2 release experiment. Int. J. Greenhouse Gas Control (in the Special Issue on STEMM-CCS).

French McCay, D., Jayko, K., Li, Z., Horn, M., Kim, Y., Isaji, T., Crowley, D., Spaulding, M., Decker, L., Turner, C., Zamorski, S., Fontenault, J., Shmookler, R., Rowe, J., 2015. Technical Reports For *Deepwater Horizon* Water Column Injury Assessment WC_TR.14: Modeling oil Fate and Exposure Concentrations in the Deepwater Plume and Rising Oil Resulting from the *Deepwater Horizon* Oil Spill. RPS ASA, South Kingstown.

Gros, J., Arey, J.S., Socolofsky, S.A., Dissanayake, A.L., 2020. Dynamics of live oil droplets and natural gas bubbles in deep water. Environ. Sci. Technol. https://doi.org/10.1021/acs.est.9b06242.

Gros, J., Reddy, C.M., Nelson, R.K., Socolofsky, S.A., Arey, J.S., 2016. Simulating gas–liquid–water partitioning and fluid properties of petroleum under pressure: implications for deep-sea blowouts. Environ. Sci. Technol. 50, 7397–7408. https://doi.org/10.1021/acs.est.5b04617.

Gros, J., Schmidt, M., Dale, A.W., Linke, P., Vielstädte, L., Bigalke, N., Haeckel, M., Wallmann, K., Sommer, S., 2019. Simulating and quantifying multiple natural subsea CO_2 seeps at Panarea Island (Aeolian Islands, Italy) as a proxy for potential leakage from subseabed carbon storage sites. Environ. Sci. Technol. 53, 10258–10268. https://doi.org/10.1021/acs.est.9b02131.

Gros, J., Socolofsky, S.A., Dissanayake, A.L., Jun, I., Zhao, L., Boufadel, M.C., Reddy, C. M., Arey, J.S., 2017. Petroleum dynamics in the sea and influence of subsea dispersant injection during *Deepwater Horizon*. Proc. Natl. Acad. Sci., 201612518 https://doi.org/10.1073/pnas.1612518114.

Hamme, R.C., Emerson, S.R., 2004. The solubility of neon, nitrogen and argon in distilled water and seawater. Deep Sea Res. Part Oceanogr. Res. Pap. 51, 1517–1528. https://doi.org/10.1016/j.dsr.2004.06.009.

Hepple, R.P., Benson, S.M., 2005. Geologic storage of carbon dioxide as a climate change mitigation strategy: performance requirements and the implications of surface seepage. Environ. Geol. 47, 576–585. https://doi.org/10.1007/s00254-004-1181-2.

Holtappels, M., Lorke, A., 2011. Estimating turbulent diffusion in a benthic boundary layer. Limnol. Oceanogr. Methods 9, 29–41. https://doi.org/10.4319/lom.2011.9.29.

IPCC, 2005. Carbon Dioxide Capture and Storage: Special Report of the Intergovernmental Panel On Climate Change, Intergovernmental Panel on Climate Change. Cambridge University Press, New York.

IPCC, 2018. Global warming of 1.5°C, An IPCC special report on the impacts of global warming of 1.5°C above pre-industrial levels and related global greenhouse gas emission pathways, in the context of strengthening the global response to the threat of climate change, sustainable development, and efforts to eradicate poverty. In: Global warming of 1.5°C, An IPCC special report on the impacts of global warming of 1.5°C above pre-industrial levels and related global greenhouse gas emission pathways, in the context of strengthening the global response to the threat of climate change, sustainable development, and efforts to eradicate poverty (No. IPCC SR 1.5). IPCC, Geneva, Switzerland.

Johnson, A.I., Besik, F., Hamielec, A.E., 1969. Mass transfer from a single rising bubble. Can. J. Chem. Eng. 47, 559–564.

Jun, I., 2018. A Numerical Model For Hydrocarbon Bubbles from Natural Seeps Within Hydrate Stability Zone. Texas A&M University, College Station, Texas. Ph.D. Dissertation.

Koopmans, D., Meyer, V., Holtappels, M., Schaap, A., Dewar, W., Färber, P., Long, M., Gros, J., Connelly, D., de Beer, D., 2021. Detection and quantification of a release of carbon dioxide gas at the seafloor using pH eddy covariance and measurements of plume advection. Int. J. Greenhouse Gas Control (in the Special Issue on STEMM-CCS).

Leifer, I., 2019. A synthesis review of emissions and fates for the Coal Oil Point marine hydrocarbon seep field and California marine seepage. Geofluids 48. https://doi.org/10.1155/2019/4724587.

Leifer, I., Culling, D., 2010. Formation of seep bubble plumes in the Coal Oil Point seep field. Geo-Mar. Lett. 30, 339–353. https://doi.org/10.1007/s00367-010-0187-x.

Leonte, M., Wang, B., Socolofsky, S.A., Mau, S., Breier, J.A., Kessler, J.D., 2018. Using carbon isotope fractionation to constrain the extent of methane dissolution into the water column surrounding a natural hydrocarbon gas seep in the northern Gulf of Mexico. Geochem. Geophys. Geosystems 19, 4459–4475. https://doi.org/10.1029/2018GC007705.

Li, J., White, P.R., Roche, B., Bull, J.M., Leighton, T.G., Davis, J.W., Fone, J.W., 2021. Acoustic and optical determination of bubble size distributions - Quantification of seabed gas emissions. Int. J. Greenh. Gas Control 108, 103313. https://doi.org/10.1016/j.ijggc.2021.103313.

Lichtschlag, A., Haeckel, M., Olierook, D., Peel, K., Flohr, A., Pearce, C.R., Marieni, C., James, R.H., Stahl, H., Connelly, D.P., 2021. Impact of CO_2 leakage from sub-seabed carbon dioxide storage on sediment and porewater geochemistry. Int. J. Greenhouse Gas Control (in the Special Issue on STEMM-CCS).

Linke, P., Schmidt, M., Rohleder, M., Al-Barakati, A., Al-Farawati, R., 2015. Novel online digital video and high-speed data broadcasting via standard coaxial cable onboard marine operating vessels. Mar. Technol. Soc. J. 49, 7–18. https://doi.org/10.4031/MTSJ.49.1.2.

Liu, L., 2019. Mechanisms of Methane Bubble Formation, Storage and Release in Freshwater Sediments. Universität Koblenz-Landau. Ph.D. Dissertation.

Liu, L., De Kock, T., Wilkinson, J., Cnudde, V., Xiao, S., Buchmann, C., Uteau, D., Peth, S., Lorke, A., 2018. Methane bubble growth and migration in aquatic sediments observed by X-ray μCT. Environ. Sci. Technol. 52, 2007–2015. https://doi.org/10.1021/acs.est.7b06061.

Liu, L., Wilkinson, J., Koca, K., Buchmann, C., Lorke, A., 2016. The role of sediment structure in gas bubble storage and release. J. Geophys. Res. Biogeosciences 121, 1992–2005. https://doi.org/10.1002/2016JG003456.

Lohrberg, A., Schmale, O., Ostrovsky, I., Niemann, H., Held, P., Schneider von Deimling, J., 2020. Discovery and quantification of a widespread methane ebullition event in a coastal inlet (Baltic Sea) using a novel sonar strategy. Sci. Rep. 10, 4393. https://doi.org/10.1038/s41598-020-60283-0.

Martens, C.S., Val Klump, J., 1984. Biogeochemical cycling in an organic-rich coastal marine basin 4. An organic carbon budget for sediments dominated by sulfate reduction and methanogenesis. Geochim. Cosmochim. Acta 48, 1987–2004. https://doi.org/10.1016/0016-7037(84)90380-6.

Martínez-Cabanas, M., Esposito, M., Gros, J., Linke, P., Schmidt, M., Triest, J., Achterberg, E.P., 2021. Deviations from environmental baseline: Detection of subsea CO_2 release in the water column from real-time measurements at a potential offshore carbon dioxide storage site. Int. J. Greenh. Gas Control. 109, 103369. https://doi.org/10.1016/j.ijggc.2021.103369.

McGinnis, D.F., Greinert, J., Artemov, Y., Beaubien, S.E., Wüest, A., 2006. Fate of rising methane bubbles in stratified waters: how much methane reaches the atmosphere? J. Geophys. Res. Oceans 111, C09007. https://doi.org/10.1029/2005JC003183.

McGinnis, D.F., Schmidt, M., DelSontro, T., Themann, S., Rovelli, L., Reitz, A., Linke, P., 2011. Discovery of a natural CO_2 seep in the German North Sea: implications for shallow dissolved gas and seep detection. J. Geophys. Res. Oceans 116. https://doi.org/10.1029/2010JC006557.

McGinnis, D.F., Sommer, S., Lorke, A., Glud, R.N., Linke, P., 2014. Quantifying tidally driven benthic oxygen exchange across permeable sediments: an aquatic eddy correlation study. J. Geophys. Res. Oceans 119, 6918–6932. https://doi.org/10.1002/2014JC010303.

Millero, F.J., 2007. The marine inorganic carbon cycle. Chem. Rev. 107, 308–341. https://doi.org/10.1021/cr0503557.

Miloshevich, L.M., Paukkunen, A., Vömel, H., Oltmans, S.J., 2004. Development and validation of a time-lag correction for Vaisala radiosonde humidity measurements. J. Atmospheric Ocean. Technol. 21, 1305–1327. https://doi.org/10.1175/1520-0426(2004)021<1305:DAVOAT>2.0.CO;2.

Molari, M., Guilini, K., Lott, C., Weber, M., de Beer, D., Meyer, S., Ramette, A., Wegener, G., Wenzhöfer, F., Martin, D., Cibic, T., Vittor, C.D., Vanreusel, A., Boetius, A., 2018. CO_2 leakage alters biogeochemical and ecological functions of submarine sands. Sci. Adv. 4, eaao2040. https://doi.org/10.1126/sciadv.aao2040.

Okubo, A., 1972. Some speculations on oceanic diffusion diagrams. In: Symposium on "The Physical Processes Responsible for the Dispersal of Pollutants in the Sea with Special Reference to the Nearshore Zone".

Oldenburg, C.M., Pan, L., 2019. Major CO_2 blowouts from offshore wells are strongly attenuated in water deeper than 50m. Greenh. Gases Sci. Technol. n/a 1–17. https://doi.org/10.1002/ghg.1943.

Olsen, J.E., Dunnebier, D., Davies, E., Skjetne, P., Morud, J., 2017. Mass transfer between bubbles and seawater. Chem. Eng. Sci. 161, 308–315. https://doi.org/10.1016/j.ces.2016.12.047.

Olsen, J.E., Krause, D.F., Davies, E.J., Skjetne, P., 2019. Observations of rising methane bubbles in Trondheimsfjord and its implications to gas dissolution. J. Geophys. Res. Oceans 124, 1399–1409. https://doi.org/10.1029/2018JC013978.

Orr, J.C., Epitalon, J.-.M., Dickson, A.G., Gattuso, J.-.P., 2018. Routine uncertainty propagation for the marine carbon dioxide system. Mar. Chem. 207, 84–107. https://doi.org/10.1016/j.marchem.2018.10.006.

Phelps, J.J.C., Blackford, J.C., Holt, J.T., Polton, J.A., 2015. Modelling large-scale CO_2 leakages in the North Sea. Int. J. Greenh. Gas Control, CCS and the Marine Environment 38, 210–220. https://doi.org/10.1016/j.ijggc.2014.10.013.

Pilson, M.E.Q., 2013. An Introduction to the Chemistry of the Sea, 2nd Ed. Cambridge University Press, Cambridge.

Razaz, M., Di Iorio, D., Wang, B., Daneshgar Asl, S., Thurnherr, A.M., 2020. Variability of a natural hydrocarbon seep and its connection to the ocean surface. Sci. Rep. 10, 12654. https://doi.org/10.1038/s41598-020-68807-4.

Rehder, G., Leifer, I., Brewer, P.G., Friederich, G., Peltzer, E.T., 2009. Controls on methane bubble dissolution inside and outside the hydrate stability field from open ocean field experiments and numerical modeling. Mar. Chem. 114, 19–30. https://doi.org/10.1016/j.marchem.2009.03.004.

Ringrose, P.S., Meckel, T.A., 2019. Maturing global CO_2 storage resources on offshore continental margins to achieve 2DS emissions reductions. Sci. Rep. 9, 17944. https://doi.org/10.1038/s41598-019-54363-z.

Roberts, J.J., Gilfillan, S.M.V., Stalker, L., Naylor, M., 2017. Geochemical tracers for monitoring offshore CO_2 stores. Int. J. Greenh. Gas Control 65, 218–234. https://doi.org/10.1016/j.ijggc.2017.07.021.

Roche, B., Bull, J.M., Marin-Moreno, H., Leighton, T.G., Falcon-Suarez, I.H., Tholen, M., White, P.R., Provenzano, G., Lichtschlag, A., Li, J., Faggetter, M., 2021. Time-lapse imaging of CO_2 migration within near-surface sediments during a controlled sub-seabed release experiment. Int. J. Greenh. Gas Control. 109, 103363.

Römer, M., Riedel, M., Scherwath, M., Heesemann, M., Spence, G.D., 2016. Tidally controlled gas bubble emissions: a comprehensive study using long-term monitoring data from the NEPTUNE cabled observatory offshore Vancouver Island. Geochem. Geophys. Geosystems 17, 3797–3814. https://doi.org/10.1002/2016GC006528.

Römer, M., Sahling, H., Pape, T., Bohrmann, G., Spieß, V., 2012. Quantification of gas bubble emissions from submarine hydrocarbon seeps at the Makran continental margin (offshore Pakistan). J. Geophys. Res. Oceans 117. https://doi.org/10.1029/2011JC007424.

Ross, O.N., Sharples, J., 2004. Recipe for 1-D Lagrangian particle tracking models in space-varying diffusivity. Limnol. Oceanogr. Methods 2, 289–302. https://doi.org/10.4319/lom.2004.2.289.

Rovelli, L., Dengler, M., Schmidt, M., Sommer, S., Linke, P., McGinnis, D.F., 2016. Thermocline mixing and vertical oxygen fluxes in the stratified central North Sea. Biogeosciences 13, 1609–1620. https://doi.org/10.5194/bg-13-1609-2016.

Schaap, A., Koopmans, D., Holtappels, M., Dewar, M., Arundell, M., Papadimitriou, S., Hanz, R., Monk, S., Mowlem, M., Loucaides, S., 2021. Quantification of a subsea CO_2 release with lab-on-chip sensors measuring benthic gradients. Int. J. Greenhouse Gas Control (in the Special Issue on STEMM-CCS).

Schmidt, M., 2019. Cruise Report POS534 STEMM-CCS (GEOMAR Report No. 52). GEOMAR Helmholtz-Zentrum für Ozeanforschung, Kiel, Germany. https://doi.org/10.3289/geomar_rep_ns_52_2019.

Schmidt, M., Linke, P., Sommer, S., Esser, D., Cherednichenko, S., 2015. Natural CO_2 seeps offshore Panarea: a test site for subsea CO_2 leak detection technology. Mar. Technol. Soc. J. 49, 19–30 https://doi.org/info:doi/10.4031/MTSJ.49.1.3.

Schulz, K.G., Riebesell, U., Rost, B., Thoms, S., Zeebe, R.E., 2006. Determination of the rate constants for the carbon dioxide to bicarbonate inter-conversion in pH-buffered seawater systems. Mar. Chem. 100, 53–65. https://doi.org/10.1016/j.marchem.2005.11.001.

Schulze, G., Schlünder, E.U., 1985. Physical absorption of single gas bubbles in degassed and preloaded water. Chem. Eng. Process. Process Intensif. 19, 27–37. https://doi.org/10.1016/0255-2701(85)80002-7.

Sellami, N., Dewar, M., Stahl, H., Chen, B., 2015. Dynamics of rising CO_2 bubble plumes in the QICS field experiment: part 1 – the experiment. Int. J. Greenh. Gas Control, CCS Marine Environ. 38, 44–51. https://doi.org/10.1016/j.ijggc.2015.02.011.

Sharqawy, M.H., Lienhard, J.H., Zubair, S.M., 2010. Thermophysical properties of seawater: a review of existing correlations and data. Desalination Water Treat 16, 354–380. https://doi.org/10.5004/dwt.2010.1079.

Socolofsky, S.A., Adams, E.E., 2002. Multi-phase plumes in uniform and stratified crossflow. J. Hydraul. Res. 40, 661–672. https://doi.org/10.1080/00221680209499913.

Socolofsky, S.A., Gros, J., 2019. Report on Deepwater Horizon simulations with different droplet size distributions, Appendix E consultant's report. In: The Use of Dispersants in Marine Oil Spill Response, 410 p.

Socolofsky, S.A., Wang, B., Kim, B., Jun, I., 2020. Dynamic Behavior of Natural Seep Vents: Analysis of Field and Laboratory Observations and Modeling (Final Scientific/Technical Report). National Energy Technology Laboratory.

Sommer, S., Schmidt, M., Linke, P., 2015. Continuous inline mapping of a dissolved methane plume at a blowout site in the Central North Sea UK using a membrane inlet mass spectrometer – Water column stratification impedes immediate methane release into the atmosphere. Mar. Pet. Geol. 68, 766–775. https://doi.org/10.1016/j.marpetgeo.2015.08.020.

Taylor, P., Stahl, H., Vardy, M.E., Bull, J.M., Akhurst, M., Hauton, C., James, R.H., Lichtschlag, A., Long, D., Aleynik, D., Toberman, M., Naylor, M., Connelly, D., Smith, D., Sayer, M.D.J., Widdicombe, S., Wright, I.C., Blackford, J., 2015. A novel sub-seabed CO_2 release experiment informing monitoring and impact assessment for geological carbon storage. Int. J. Greenh. Gas Control, CCS Marine Environ. 38, 3–17. https://doi.org/10.1016/j.ijggc.2014.09.007.

Torres, M.E., McManus, J., Hammond, D.E., de Angelis, M.A., Heeschen, K.U., Colbert, S.L., Tryon, M.D., Brown, K.M., Suess, E., 2002. Fluid and chemical fluxes in and out of sediments hosting methane hydrate deposits on Hydrate Ridge, OR, I: hydrological provinces. Earth Planet. Sci. Lett. 201, 525–540. https://doi.org/10.1016/S0012-821X(02)00733-1.

Totland, C., Eek, E., Blomberg, A.E.A., Waarum, I.-.K., Fietzek, P., Walta, A., 2020. The correlation between pO_2 and pCO_2 as a chemical marker for detection of offshore CO_2 leakage. Int. J. Greenh. Gas Control 99, 103085. https://doi.org/10.1016/j.ijggc.2020.103085.

Uchimoto, K., Nishimura, M., Watanabe, Y., Xue, Z., 2020. An experiment revealing the ability of a side-scan sonar to detect CO_2 bubbles in shallow seas. Greenh. Gases Sci. Technol. 10, 591–603. https://doi.org/10.1002/ghg.1991.

Veloso, M., Greinert, J., Mienert, J., Batist, M.D., 2015. A new methodology for quantifying bubble flow rates in deep water using splitbeam echosounders: examples from the Arctic offshore NW-Svalbard. Limnol. Oceanogr. Methods 13, 267–287. https://doi.org/10.1002/lom3.10024.

Vielstädte, L., Karstens, J., Haeckel, M., Schmidt, M., Linke, P., Reimann, S., Liebetrau, V., McGinnis, D.F., Wallmann, K., 2015. Quantification of methane emissions at abandoned gas wells in the Central North Sea. Mar. Pet. Geol. 68, 848–860. https://doi.org/10.1016/j.marpetgeo.2015.07.030.

Vielstädte, L., Linke, P., Schmidt, M., Sommer, S., Haeckel, M., Braack, M., Wallmann, K., 2019. Footprint and detectability of a well leaking CO_2 in the Central North Sea: implications from a field experiment and numerical modelling. Int. J. Greenh. Gas Control 84, 190–203.

Wallmann, K., Haeckel, M., Linke, P., Haffert, L., Schmidt, M., Buenz, S., James, R., Hauton, C., Tsimplis, M., Widdicombe, S., Blackford, J., Queiros, A.M., Connelly, D., Lichtschlag, A., Dewar, M., Chen, B., Baumberger, T., Beaubin, S., Vercelli, S., Proelss, A., Wildenborg, T., Mikunda, T., Nepveu, M., Maynard, C., Finnerty, S., Flach, T., Ahmed, N., Ulfsnes, A., Brooks, L., Moskeland, T., Purcell, M., 2015. Best Practice Guidance For Environmental Risk Assessment For Offshore CO_2 Geological Storage (ECO2 Deliverable No. D14.1). ECO2 Project Office, Kiel, Germany http://dx.doi.org/10.3289/ECO2_D14.1.

Wang, B., Jun, I., Socolofsky, S.A., DiMarco, S.F., Kessler, J.D., 2020. Dynamics of gas bubbles from a submarine hydrocarbon seep within the hydrate stability zone. Geophys. Res. Lett. 47, e2020GL089256 https://doi.org/10.1029/2020GL089256.

Wang, B., Socolofsky, S.A., 2015. A deep-sea, high-speed, stereoscopic imaging system for in situ measurement of natural seep bubble and droplet characteristics. Deep Sea Res. Part Oceanogr. Res. Pap. 104, 134–148. https://doi.org/10.1016/j.dsr.2015.08.001.

Wang, B., Socolofsky, S.A., Lai, C.C.K., Adams, E.E., Boufadel, M.C., 2018. Behavior and dynamics of bubble breakup in gas pipeline leaks and accidental subsea oil well blowouts. Mar. Pollut. Bull. 131, 72–86. https://doi.org/10.1016/j.marpolbul.2018.03.053. Part A.

Weber, U.W., Kipfer, R., Horstmann, E., Ringrose, P., Kampman, N., Tomonaga, Y., Brennwald, M.S., Sundal, A., 2021. Noble gas tracers in gas streams at Norwegian CO_2 capture plants. Int. J. Greenh. Gas Control 106, 103238. https://doi.org/10.1016/j.ijggc.2020.103238.

Wüest, A., Brooks, N.H., Imboden, D.M., 1992. Bubble plume modeling for lake restoration. Water Resour. Res. 28, 3235–3250. https://doi.org/10.1029/92WR01681.

Wüest, A., Piepke, G., Senden, D.C.V., 2000. Turbulent kinetic energy balance as a tool for estimating vertical diffusivity in wind-forced stratified waters. Limnol. Oceanogr. 45, 1388–1400. https://doi.org/10.4319/lo.2000.45.6.1388.

Zeebe, R., Wolf-Gladrow, D., 2001. CO_2 in Seawater: Equilibrium, Kinetics, Isotopes. In: Elsevier Oceanography Series, 65. Elsevier, Amsterdam.

Zheng, L., Yapa, P.D., 2002. Modeling gas dissolution in deepwater oil/gas spills. J. Mar. Syst. 31, 299–309. https://doi.org/10.1016/S0924-7963(01)00067-7.